Sense and Sensitivity - I. Uncertainty analysis of the gas-phase chemistry in AGB outflows

M. Van de Sande, 1* M. Gueguen, 2 T. Danilovich, 3,4 T. J. Millar 5

- ¹Leiden Observatory, Leiden University, P.O. Box 9513, 2300 RA Leiden, The Netherlands
- ²Laboratoire CAPHI, University of Rennes, Rue du Thabor 2, 35000 Rennes, France
- ³School of Physics & Astronomy, Monash University, Wellington Road, Clayton 3800, Victoria, Australia
- ⁴Institute of Astronomy, KU Leuven, Celestijnenlaan 200D, 3001 Leuven, Belgium
- ⁵Astrophysics Research Centre, School of Mathematics and Physics, Queen's University Belfast, University Road, Belfast BT7 1NN, UK

Accepted XXX. Received YYY; in original form ZZZ

ABSTRACT

Chemical reaction networks are central to all chemical models. Each rate coefficient has an associated uncertainty, which is generally not taken into account when calculating the chemistry. We performed the first uncertainty analysis of a chemical model of C-rich and O-rich AGB outflows using the RATE22 reaction network. Quantifying the error on the model predictions enables us to determine the need for adding complexity to the model. Using a Monte Carlo sampling method, we quantified the impact of the uncertainties on the chemical kinetic data on the predicted fractional abundances and column densities. The errors are caused by a complex interplay of reactions forming and destroying each species. Parent species show an error on their envelope sizes, which is not caused by the uncertainty on their photodissociation rate, but rather the chemistry reforming the parent after its photodissociation. Using photodissociation models to estimate the envelope size might be an oversimplification. The error on the CO envelope impacts retrieved mass-loss rates by up to a factor of two. For daughter species, the error on the peak fractional abundance ranges from a factor of a few to three orders of magnitude, and is on average about 10% of its value. This error is positively correlated with the error on the column density. The standard model suffices for many species, e.g., the radial distribution of cyanopolyynes and hydrocarbon radicals around IRC+10216. However, including spherical asymmetries, dust-gas chemistry, and photochemistry induced by a close-by stellar companion are still necessary to explain certain observations.

Key words: astrochemistry – molecular processes – circumstellar matter – stars: AGB and post-AGB – ISM: molecules

1 INTRODUCTION

The outflows of asymptotic giant branch (AGB) stars are rich astrochemical environments, with around 130 different molecules and some 15 types of newly formed dust species detected so far (Decin 2021). The type of chemistry in the outflow is set by the star's elemental carbon-to-oxygen ratio (C/O), where stars with C/O < 1 have O-rich outflows and stars with C/O > 1 have C-rich outflows. Asymmetrical structures are observed to be ubiquitous within their circumstellar envelopes (CSEs), ranging from small-scale structures close to the star, likely caused by its convective motion (Khouri et al. 2016; Wittkowski et al. 2017; Velilla-Prieto et al. 2023), and large-scale structures such as spirals (e.g., Mauron & Huggins 2006; Maercker et al. 2016) and disks (e.g., Kervella et al. 2016; Homan et al. 2018; Safonov et al. 2025), which are thought to be caused by binary interaction with a (sub)stellar companion (Decin et al. 2020). Chemical kinetics models are crucial to understand the close link between chemistry and dynamics throughout the outflow and are essential to interpret the observed abundance distributions.

The most widely used chemical model of AGB outflows describes the gas-phase chemistry from the inner wind outwards, assuming

* E-mail: mvdsande@strw.leidenuniv.nl

a spherically symmetric outflow with constant expansion velocity (e.g., Goldreich & Scoville 1976; Scalo & Slavsky 1980; Agúndez & Cernicharo 2006; McElroy et al. 2013). This standard CSE model has successfully explained several observations, especially those of the photochemistry-dominated outer regions of the outflow (e.g., Huggins & Glassgold 1982; Nejad et al. 1984; Cherchneff & Glassgold 1993; Millar et al. 2000; Li et al. 2016). Nevertheless, important discrepancies with observations remain.

Additional physics and chemistry has been included in the standard model to better understand observations. (i) Small- and large-scale density structures impact the radiation field throughout the outflow, allowing interstellar UV photons to reach the inner wind. These are included in the 1D model by allowing a set fraction of photons to reach the inner wind uninhibited (Agúndez et al. 2010) or by using the porosity formalism, where the change in opacity of the outflow depends on its specific clumpiness (Van de Sande et al. 2018). The impact of close-by stellar companions depends on the type of companion and the density structure of the outflow, where the outflow can appear either molecule-poor or show an increase in chemical complexity (Van de Sande & Millar 2022). The model can account for the detection of HC₃N close to IRC+10216 (Siebert et al. 2022) and that of SiC and SiN in the inner wind of W Aql (Danilovich et al. 2024). (iii) The chemical network can be extended to include simplified dust-gas chemistry (Jura & Morris 1985; Charnley & Smith 1993; Dijkstra et al. 2003, 2006) or comprehensive dust-gas and grain-surface chemistry (Van de Sande et al. 2019, 2020, 2021). This allows for the formation of ices on dust, in particular H₂O ice as observed around OH/IR stars (Sylvester et al. 1999), and corroborates the observed depletion of SiO and SiS in high-density O-rich outflows (González Delgado et al. 2003; Bujarrabal et al. 1989; Decin et al. 2010) and trends in the abundance of refractory species with outflow density (González Delgado et al. 2003; Massalkhi et al. 2019, 2020). The three layers of complexity described above can be combined, which reveals degeneracies in the model predictions (Van de Sande et al. 2023). Including (a combination of) physical and chemical complexities changes the model predictions and improves the agreement with observed abundance profiles.

Chemical models are used in a deterministic manner, giving one solution for a given set of certain input parameters. This includes the rate coefficients of the reactions in the chemical network, of which each has an associated uncertainty. The model predictions hence have an unknown inherent error due to the uncertainty on the kinetic data at the heart of the model. Assessing the effect of uncertainties on the kinetic data on the model predictions has been done for a variety of astrochemical environments (e.g., Dobrijevic et al. 2003; Vasyunin et al. 2004; Wakelam et al. 2005, 2006a,b; Vasyunin et al. 2008; Dobrijevic et al. 2010; Penteado et al. 2017), including IRC +10216 (Wakelam et al. 2010). Here, we present the first uncertainty analysis of the standard CSE model, investigating three different outflow densities for both C-rich and O-rich outflows. Allocating the uncertainty on the model predictions to specific reactions requires a sensitivity analysis, which will be presented in a follow-up paper.

Previously added physics and chemistry are not taken into account, but regarded as perturbations to the standard model. As we do not vary significantly over the physical description of the outflow, this study complementary to that of Maes et al. (2023), where the physics was varied but the chemistry was considered to be fixed. By quantifying the error on the model predictions due to the uncertainties on the input chemical kinetic data, we can establish the need for adding further physical and chemical complexity to the model. Furthermore, this uncertainty analysis provides insights into both the chemical model and AGB outflows themselves, inasmuch as we can determine what kind of complexities could solve which types of discrepancies with observations.

In Sect. 2, the chemical model is described along with the Monte Carlo method used. We show our results in Sect. 3, followed by the discussion and conclusions in Sect. 4 and Sect. 5.

2 CHEMICAL MODEL AND MONTE CARLO METHOD

The chemical reaction network and chemical model are described in Sects 2.1 and 2.2. The Monte Carlo sampling method used to take the uncertainties on the rate coefficients into account is described in Sect. 2.3. The methods to calculate the model predictions and their errors are described in Sect. 2.4.

2.1 The UDfA RATE22 reaction network

The chemical reaction network used is the publicly available RATE22 release of the UMIST Database for Astrochemistry (UDfA)¹, a gasphase only network containing 8767 rate coefficients involving 737 species (Millar et al. 2024). For each rate coefficient, the database

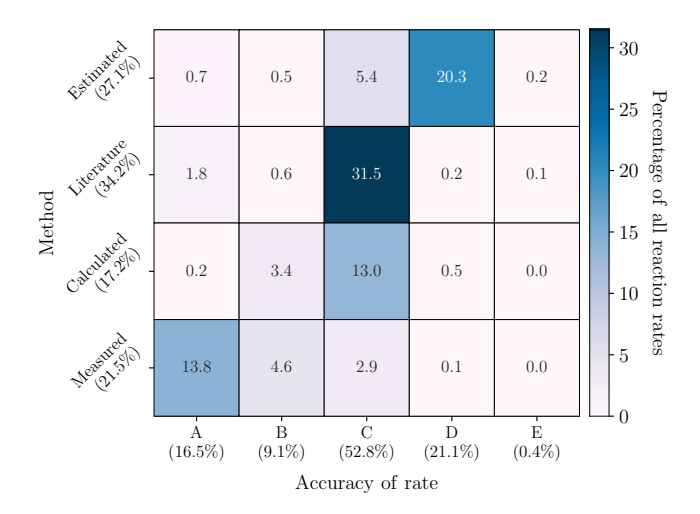


Figure 1. Distribution of the RATE22 reaction rates per associated accuracy and the method by which the rate has been determined. Percentages are indicated in colour and as printed in each category. An accuracy of A represents an error of less than 25%, B less than 50%, C within a factor of 2, D within an order of magnitude, and E a highly uncertain error The percentage of rates for each method and accuracy are indicated at each row and column, respectively.

lists the method with which it has been determined and an estimate of its accuracy. The accuracy estimate is divided into five categories, where category A represents an error of less than 25%, B an error of less than 50%, C an error within a factor of 2, D within an order of magnitude, and E a highly uncertain error.

Fig. 1 visualises the RATE22 reaction network per accuracy and per method. About one-fifth (21.5%) of all rate coefficients is measured experimentally, 17.2% of rate coefficients are calculated. The remaining ~60% of rate coefficients are either estimated or obtained from the literature (referring to coefficients harvested from published networks or when no information on the method could be determined). Only a quarter of all 8767 rate coefficients (25.6%) have an error of less than 50% (accuracy A and B). About one-third of all coefficients (31.5%) are obtained from the literature with an accuracy C (factor 2). On average, the accuracy of the coefficient decreases as the method shifts to estimate or literature. Measured coefficients are the most accurate, with the majority having an accuracy A. Most calculated coefficients have an accuracy C, most estimated coefficients have an accuracy D. Many of the rate coefficients apply only to a restricted range in temperature. Their uncertainty outside this range is unknown; we assume the same uncertainty as within the range.

The chemical reaction network is closed but is not complete, indeed no network can be complete. While great effort has gone into including new species detected over the past decade in the RATE22 network, we cannot know whether all relevant reactions are covered to sufficiently describe inter- and circumstellar chemistry. Assessing the effects of the uncertainties on the rate coefficients in the network is one of the first steps to start addressing effects of the (in)completeness of the reaction network on the model predictions.

2.2 Circumstellar envelope chemical model

We use the publicly available CSE model associated with the UDfA RATE22 release². The model describes a spherically symmetric outflow with constant mass-loss rate, \dot{M} , and expansion velocity, v_{∞} ;

¹ https://umistdatabase.net/

https://github.com/MarieVdS/rate22_cse_code

Table 1. Physical parameters of the chemical model.

Outflow density, \dot{M} - v_{∞}	$\begin{array}{c} 10^{-5} \ M_{\odot} \ yr^{-1} - 15 \ km \ s^{-1} \\ 10^{-6} \ M_{\odot} \ yr^{-1} - 10 \ km \ s^{-1} \\ 10^{-7} \ M_{\odot} \ yr^{-1} - 5 \ km \ s^{-1} \end{array}$
Stellar temperature, T_*	2000 K
Exponent $T(r)$, ϵ	-0.7
Stellar radius, R_*	2×10^{13} cm
Start of the model	4 ×10 ¹³ cm
End of the model	1 ×10 ¹⁸ cm

Table 2. Parent species and their abundances relative to H₂ for the C-rich and O-rich outflows, as derived from observations by Agúndez et al. (2020). The CO abundances were retrieved by Teyssier et al. (2006).

Car	bon-rich	Oxygen-rich			
Species	Abun.	Species	Abun.		
Не	0.17	Не	0.17		
CO	8.00×10^{-4}	CO	3.00×10^{-4}		
N_2	4.00×10^{-5}	H_2O	2.15×10^{-4}		
CH_4	3.50×10^{-6}	N_2	4.00×10^{-5}		
H_2O	2.55×10^{-6}	SiO	2.71×10^{-5}		
SiC_2	1.87×10^{-5}	H_2S	1.75×10^{-5}		
CS	1.06×10^{-5}	SO_2	3.72×10^{-6}		
C_2H_2	4.38×10^{-5}	SO	3.06×10^{-6}		
HCN	4.09×10^{-5}	SiS	9.53×10^{-7}		
SiS	5.98×10^{-6}	NH_3	6.25×10^{-7}		
SiO	5.02×10^{-6}	CO_2	3.00×10^{-7}		
HCl	3.25×10^{-7}	HCN	2.59×10^{-7}		
C_2H_4	6.85×10^{-8}	PO	7.75×10^{-8}		
NH_3	6.00×10^{-8}	CS	5.57×10^{-8}		
HCP	2.50×10^{-8}	PN	1.50×10^{-8}		
HF	1.70×10^{-8}	HC1	1.00×10^{-8}		
H_2S	4.00×10^{-9}	HF	1.00×10^{-8}		
Na	1.00×10^{-8}	Na	1.00×10^{-8}		
Mg	1.00×10^{-8}	Mg	1.00×10^{-8}		
Fe	1.00×10^{-8}	Fe	1.00×10^{-8}		

density hence falls as $1/r^2$. The gas temperature follows a power law. CO self-shielding is taken into account via a single-band approximation (Morris & Jura 1983); H₂ is assumed to be fully self-shielded.

While the RATE22 CSE model is able to include porosity and a close-by stellar companion, we only consider a smooth outflow without any internal UV photons. This standard CSE model is still most commonly used when interpreting observations or predicting observables (e.g., Huggins & Glassgold 1982; Millar & Herbst 1994; Millar et al. 2000; Li et al. 2016; Agúndez et al. 2017; Danilovich et al. 2017; Saberi et al. 2019). In our approach, changes to the physics and chemistry of the model are regarded as perturbations to the standard CSE model whose validity is not necessarily justified.

The physical model parameters are listed in Table 1. We consider a high, intermediate, and low density outflow for both C-rich and O-rich CSEs. The temperature profile is the same for all models, as are the start (at 4×10^{13} cm = $2~R_*$) and end radii (at 10^{18} cm). The standard interstellar UV field (Draine 1978) is assumed to impinge uniformly on the outside of the outflow and is attenuated by dust (McElroy et al. 2013). The radial range is sampled logarithmically with a step size of 0.03 dex, resulting in 89 radial points. The parent species, assumed to be present at the start of the model, and their initial abundances are given in Table 2. As they do not include Ca, Ti or Al, the reactions involving these atoms play no part in the uncertainty analysis. The computation time of one model is ~25 s.

2.3 Monte Carlo method of including uncertainties of the rates

To map the uncertain rate coefficient input space to the uncertain output space, we use a Monte Carlo sampling method following Dobrijevic & Parisot (1998) and Dobrijevic et al. (2003), as used by, e.g., Wakelam et al. (2005), Wakelam et al. (2006a), and Vasyunin et al. (2008). Each rate coefficient k is considered to be a random variable, following a lognormal distribution centred on the listed reaction rate k_0 . This assumption is justified in the absence of systematic errors (Thompson & Stewart 1991; Stewart & Thompson 1996). The width of the lognormal distribution is given by the reaction's uncertainty factor F, determined by the accuracy estimate of the coefficient: $\log(F) = 1.25$ for A, 1.5 for B, C for C and C and C for C for C and C for C for C for C and C for C for C for C for C and C for C for C for C and C for C for

A new set of rate coefficients is generated by randomly sampling each rate coefficient within its associated uncertainty range. For each rate coefficient *i*, the new rate coefficient is given by

$$\log k_i = \log k_{i,0} + \epsilon_i \log F_i, \tag{1}$$

where ϵ_i is a random number sampled from a normal distribution with mean of 0 and standard deviation of 1 and $k_{i,0}$ is the rate coefficient as listed in the network. We therefore adjust the total calculated rate coefficient, calculated at the local temperature of the outflow. Uncertainties on energy barriers are absorbed into the total rate coefficient. However, their values in the network are generally not independent of the choice of the pre-exponential factor, as the adopted form is most often derived from a fit to experimental or theoretical rate coefficients over a specific temperature range. Photoreaction rates are calculated at each radius, as dust attenuates the unshielded rate (computed using photo-cross-sections where available). These attenuated rates are then adjusted using Eq. 1.

By sampling each rate coefficient N times, N sets of reaction networks are generated. The value of ϵ is different for each rate coefficient and each sample. The chemical model is calculated using each new, randomly sampled reaction network, resulting in N sets of predicted abundance profiles $X_j(r)$ for each species j.

Note that local methods, such as one at a time (OAT) methods where one rate coefficient is varied over while the others are kept constant, are invalid for chemical kinetics as it is a highly non-linear problem. Such methods cannot account for the interactions between reactions and, moreover, cannot adequately explore the multi-dimensional input parameter space. Global methods, like the Monte Carlo sampling method which we use (where a OAT design is repeated for all rate coefficients), are necessary to propagate input uncertainties through the model (Saltelli et al. 2019). Other methods, such the sampling technique of Morris (1991) where the range of possible values for each parameter is sampled by a grid of equally spaced input values, can be used for chemical reaction network studies as well (Bensberg & Reiher 2024).

We generated N=10,000 reaction networks via random sampling. This sample size is large enough to ensure convergence of the model results (see Appendix B). The chemical model was calculated using each of the newly generated networks, for each of the three outflow densities and for C-rich and O-rich chemistry, resulting in $6 \times 10,000$ total models. The parent species (Table 2) are kept constant when varying the rate coefficients; we do not consider variations in the initial composition in the outflow.

2.4 Methods for model predictions

The chemical model has two outputs for each species: its fractional abundance profile X(r) w.r.t. H_2 and its column density. Sect. 2.4.1

4 Van de Sande et al.

describes the calculation of the mean and error of each output. In Sect. 2.4.2, we define the dispersion on the column density and peak fractional abundance predictions for the daughter species. In Sect. 2.4.3, we define the mean envelope size of the parent species and its error.

2.4.1 Mean value and error

The mean fractional abundance, $\langle \log X(r) \rangle$, is calculated via

$$\langle \log X(r) \rangle = \frac{1}{N} \sum_{i=0}^{N} \log X_i(r). \tag{2}$$

This is the recommended value of the model prediction, which might differ from the fiducial prediction based on the listed rate coefficients. The error on the mean abundance, $\Delta \log X(r)$, is defined by

$$\Delta \log X(r) = \frac{1}{2} \left(\log X_{\text{max}} - \log X_{\text{min}} \right), \tag{3}$$

where $[\log X_{\min}, \log X_{\max}]$ is the smallest interval that contains 95.4% of all abundance profiles. If the distribution of $\log X(r)$ is Gaussian, this interval corresponds to 2σ of the distribution. However, we do not use the standard deviation as a measure for the error, as rapid changes in abundance (e.g., the onset of photodissociation) lead to a non-Gaussian distribution of $\log X$ (Wakelam et al. 2005).

Similarly, the logarithms of the predicted column densities also do not always follow a Gaussian distribution. We therefore use Eqs (2) and (3) to calculate the mean column density and its error. Such deviations from a Gaussian distribution are illustrated in Appendix A for both fractional abundance profiles and column densities.

2.4.2 Dispersion of column density and peak abundance

To quantify the precision of the model predictions, we use their dispersion given by

Dispersion =
$$\frac{\text{Mean}}{\text{Error}} \times 100\%$$
, (4)

where the mean and error are obtained from Eqs (2) and (3). The dispersion is hence a measure of the spread of the predicted values around their mean value. A smaller dispersion corresponds to a larger precision of the model predictions. Note that this is not equal to a higher accuracy, as the true value of the model is unknown.

The dispersion can be calculated at each radius of the fractional abundance profiles. We focus on the dispersion of the peak abundance both for feasibility of the analysis and relevance to observations. This is done only for the daughter species. We divide them into two groups: (i) *all* daughters with a column density of at least 10^5 cm⁻², removing all species that do not contribute to the overall chemistry, and (ii) the *abundant* daughters, which we define as having a peak fractional abundance of at least 10^{-10} w.r.t. H_2 and a column density of at least 10^{12} cm⁻². Within each group, we define the least precise (most uncertain) daughter species as those with dispersions larger than the mean dispersion plus one standard deviation for both peak abundance and column density. Similarly, the most precise (least uncertain) daughters are those with dispersions larger than the mean dispersion minus one standard deviation.

2.4.3 Envelope sizes of parent species

Similar dispersions are not calculated for the parent species. Their peak abundances are simply the input abundance at the start of the model, which also dominates their column densities. For the parent species, the variation on the predicted envelope size is more meaningful. The mean envelope size is measured by determining the radius where the mean fractional abundance $\langle \log X(r) \rangle$ has decreased by a factor $\log e$. Its radial extent corresponds to the radii where $\langle \log X(r) \pm \Delta \log X(r) \rangle$ has decreased by a factor $\log e$. These values correspond to the recommended value of the predicted envelope size and its error.

As a measure of the precision of the envelope, we use the range in radial extent, defined as the ratio between the largest and smallest predicted radial extents. We consider an envelope extent to be wellconstrained if this range is smaller than a factor three.

3 RESULTS

Uncertainties on the kinetic data affect both the column density and abundance predictions, resulting in errors on the model output. Parent and daughter species are influenced in different ways. Their results are shown in Sects 3.1 and 3.2, respectively.

3.1 Uncertainty on parents' molecular envelope sizes

Fig. 2 shows the mean fractional abundance profiles and their errors for the C-rich and O-rich parents in an outflow with $\dot{M}=10^{-6}~\rm M_{\odot}~\rm yr^{-1}$. In the inner wind, their predicted abundances are unaffected by the uncertainties on the reaction rates. Significant errors appear only after the onset photodissociation, leading to a spread in envelope size.

In O-rich outflows (bottom panel, Fig. 2), the abundance profiles of SO, SiS, and to a lesser extent SO_2 show an increase in abundance before photodissociation destroys them. This bump is facilitated by OH, the photodissociation product of the parent H_2O which peaks at this location. The increase in SO is caused by OH + S, where additional S is released from the parent H_2S . SO_2 is formed via OH + SO, but the bump is not as pronounced as it photodissociates into SO. The increase in SiS is mostly due to SO + Si, with some contribution of $SO_2 + Si$, where Si is mostly formed by the photodissociation of the parent SiO.

Fig. 3 shows the mean envelope sizes and radial extents together with the fiducial sizes for C-rich and O-rich outflows for all outflow densities. The values are listed in Table C1. The fiducial envelope sizes do not differ significantly from the mean predicted size; the discrepancy is larger than a factor 1.5 only for CS in O-rich outflows. As expected, the envelopes shift outward with increasing mass-loss rate. The mean envelope size is set by the onset of photodissociation, shifting the envelope outward with increasing outflow density. For each outflow density, the relative locations of the envelopes are determined by their specific photodissociation rates: the larger the rate, the smaller the envelope.

The radial extent of the envelope depends both on the species and the chemistry of the outflow. Envelope sizes that are not well-constrained, with a range in extent larger than a factor three, are indicated by a triangle. These are CO, N₂, and CS for both C-rich and O-rich outflows, SiO, SiS, PO, and PN for O-rich outflows, and HCP for C-rich outflows. The error on the envelope size is not caused by uncertainty the parents' photodissociation, as their rate coefficients all have accuracy *C*. Rather, the error on the envelope size is determined by reactions reforming the parent after the onset of its photodissociation. This depends on the specific molecule and chemical composition of the outflow. Fig. 3 shows that HCN, SiO, SiS, and CS have a larger range in O-rich outflows compared than

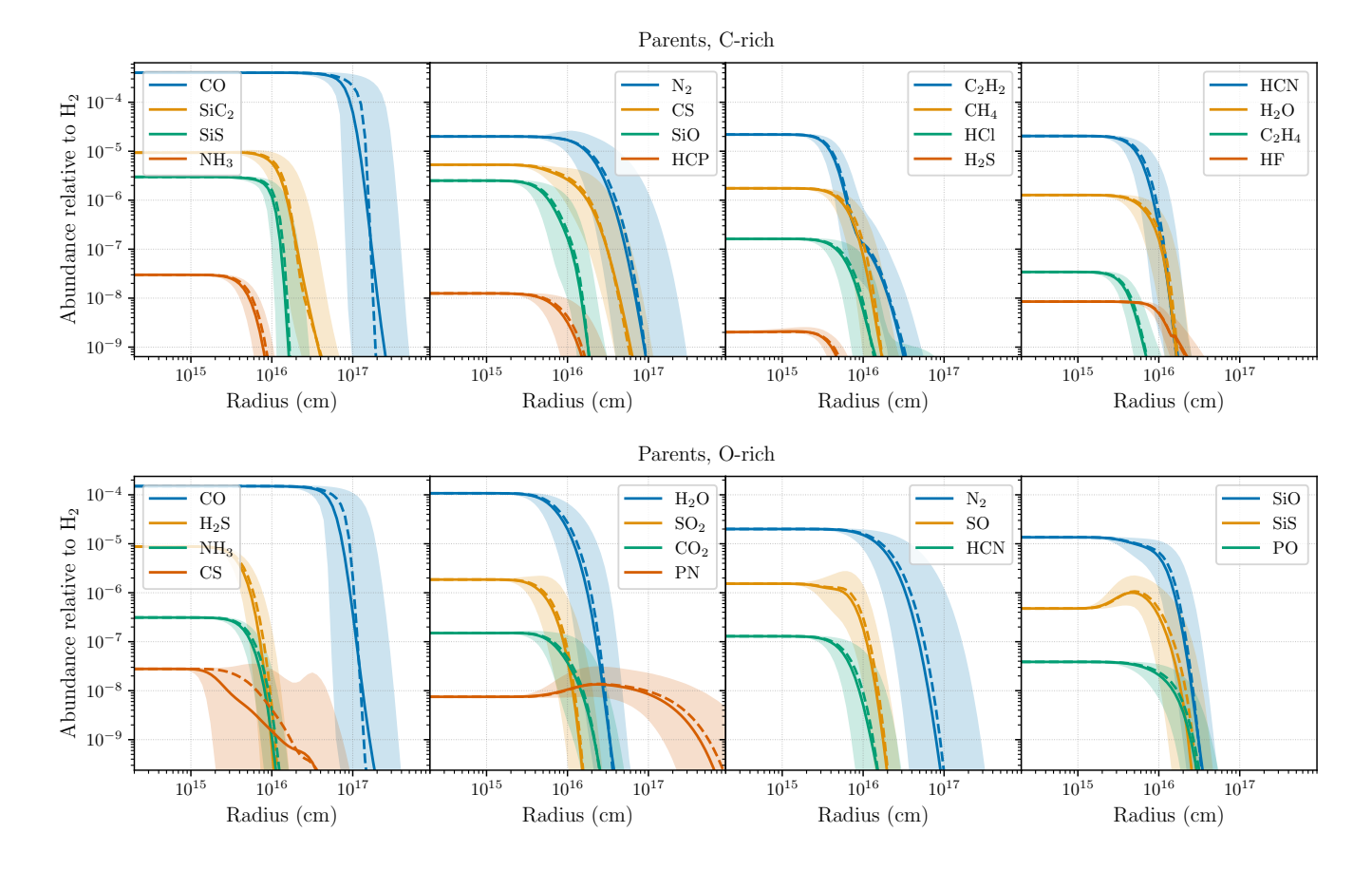


Figure 2. Fractional abundance w.r.t. H_2 of the C-rich (top) and O-rich (bottom) parent species in an outflow with $\dot{M} = 10^{-6} \, \rm M_{\odot} \, yr^{-1}$. The dashed line shows the fiducial model prediction using RATE22. The solid line shows the mean abundance $\langle \log X(r) \rangle$ of the Monte Carlo sample of reaction networks. The shaded region contains 95.4% of all predicted profiles and corresponds to the error $\Delta \log X(r)$ on the mean abundance.

Table 3. Number of daughter species in the two groups for each mass-loss rate and outflow chemistry. *All* daughter species have column density $\geq 10^5$ cm⁻². *Abundant* daughter species have peak fractional abundance $\geq 10^{-10}$ w.r.t. H₂ and column density $\geq 10^{12}$ cm⁻².

	Carb	on-rich	Oxygen-rich		
\dot{M}	All	Abun.	All	Abun.	
$10^{-5}~M_{\odot}~yr^{-1}$	529	78	201	26	
$10^{-6}~{\rm M}_{\odot}~{\rm yr}^{-1}$	520	71	193	25	
$10^{-7} \ M_{\odot} \ yr^{-1}$	506	63	181	23	

in C-rich outflows. H₂O, NH₃, H₂S and HF are well constrained for both outflows chemistries.

3.2 Uncertainty on daughter species

Table 3 lists the number of daughter species in the *all* and *abundant* daughter groups for each outflow density and composition. These are the species with a column density of at least $10^5 \ \rm cm^{-2}$, removing all species that do not contribute to the overall chemistry, and those with a peak fractional abundance of at least $10^{-10} \ \rm w.r.t.\ H_2$ and a column density of at least $10^{12} \ \rm cm^{-2}$. The number of molecules within each group increases with outflow density for both O-rich and C-rich outflows. Thanks to the reactivity of carbon, C-rich outflows have a larger number of daughters than the O-rich outflows in both categories (a factor of ~ 3 more).

In Sect. 3.2.1, we present the abundance profiles of a selection of daughter species. To condense the results, we use mean peak fractional abundances and mean column densities, their errors, and their dispersions. Sect. 3.2.2 presents the correlations between the peak fractional abundances and mean column densities and their errors, Sect. 3.2.3 presents the correlation between their dispersions and determines the most and least certain daughter species.

3.2.1 Mean abundance profiles and errors

Fig. 4 shows the mean fractional abundance profiles and their errors for a selection of daughter species in a C-rich and O-rich outflow with $\dot{M}=10^{-6}~M_{\odot}~\rm yr^{-1}$. Unlike for parent species, the predicted abundances of daughter species have a non-negligible error from the start of the model. Furthermore, the error does not necessarily grow throughout the outflow. While the error increases throughout the outflow for some species, e.g., CN and C₂H in the C-rich outflow and OH and CN in the O-rich outflow, the rate with which it increases varies throughout. Other daughters show a different behaviour. The error on, e.g., HS in the O-rich outflow and NH₂ in the C-rich outflow decreases around 10^{15} cm, after which it increases again.

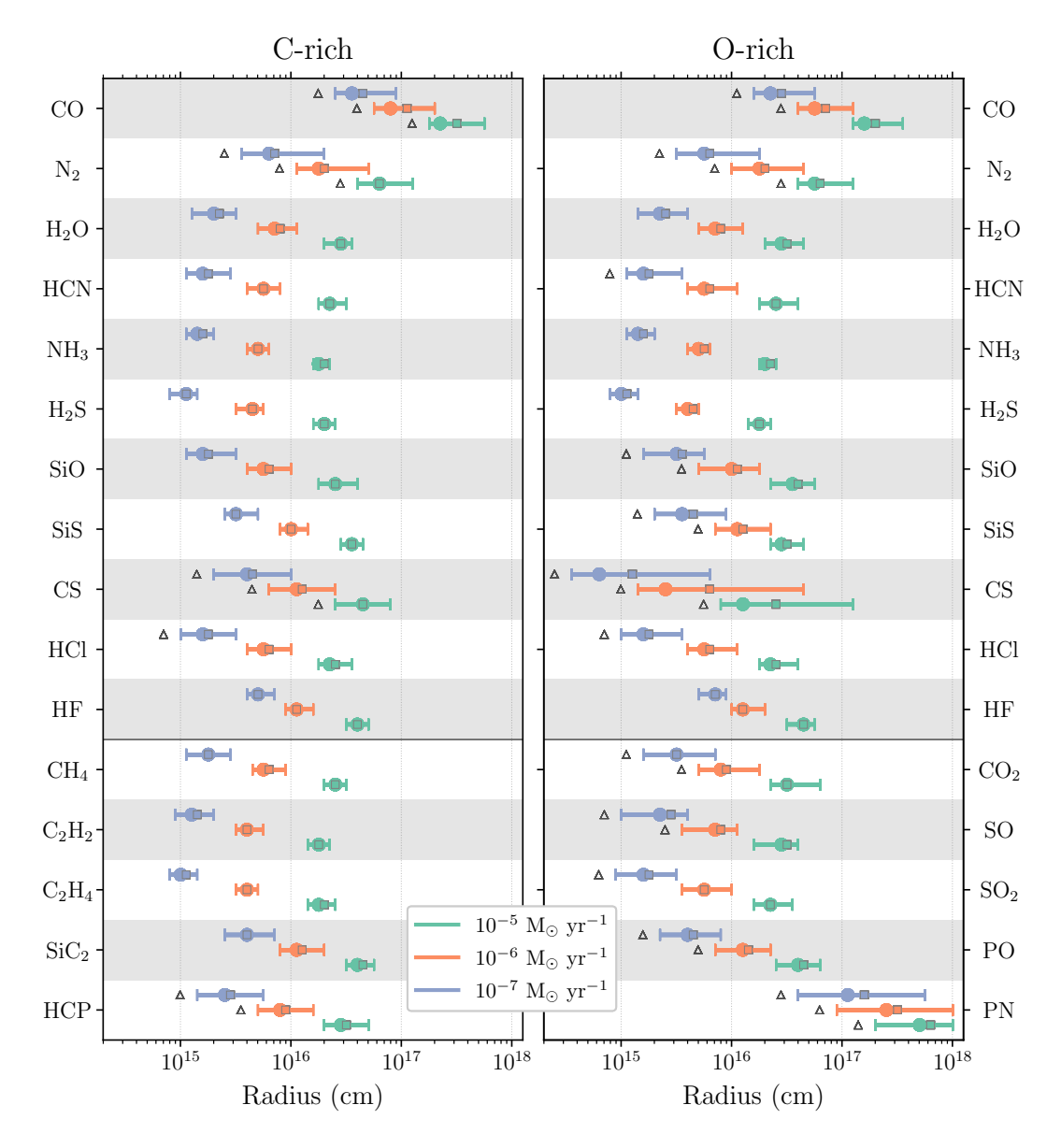


Figure 3. Envelope sizes and their radial extents for the parent species in C-rich (*left*) and O-rich (*right*) outflows. Different colours indicate different mass-loss rates. Species in common are shown near the top, differing species near the bottom. Square: envelope size as predicted using RATE22. Circle: mean envelope size obtained from the Monte Carlo sample of reaction networks. Envelopes that are not well-constrained are marked by a triangle. These have a range in radial extent (ratio between the largest and smallest radial extent) larger than 3.

3.2.2 Correlations in peak fractional abundance, column density, and their dispersions

Fig. 5 shows scatter plots of peak fractional abundance versus its error, mean column density versus its error, and dispersion of the column density versus dispersion of the peak abundance for all daughter species in a C-rich outflow with $\dot{M}=10^{-6}~\rm M_{\odot}~\rm yr^{-1}$. The peak abundances and column densities and their respective errors show a moderate negative monotonic correlation (left and middle panels). The corresponding Spearman rank correlation coefficients (RCCs) are -0.53 and -0.55, respectively. Larger values hence tend to have smaller errors. The dispersion of the column density and the dispersion of the peak fractional abundance has a moderate positive correlation (right panel, RCC = 0.44). Species with a smaller dispersion of their peak abundance also have smaller dispersions of their column density, and vice versa.

Figures D1, D2, D3, and D4 show similar scatter plots for all mass-loss rates and groups of daughter species. The corresponding RCCs and their p-values (the probability of observing a correlation as strong as or stronger than the calculated one if no correlation exists) are listed in Table D1. There is a negative correlation between peak abundance and its error and between column density and its error for both groups of daughter species, except for the abundant Orich daughters. For this subgroup, there is no statistically significant correlation, which could be due to the smaller number of abundant daughters (~25). A positive correlation between the dispersion of the peak abundance and the dispersion of the column density exists for both groups of daughter species.

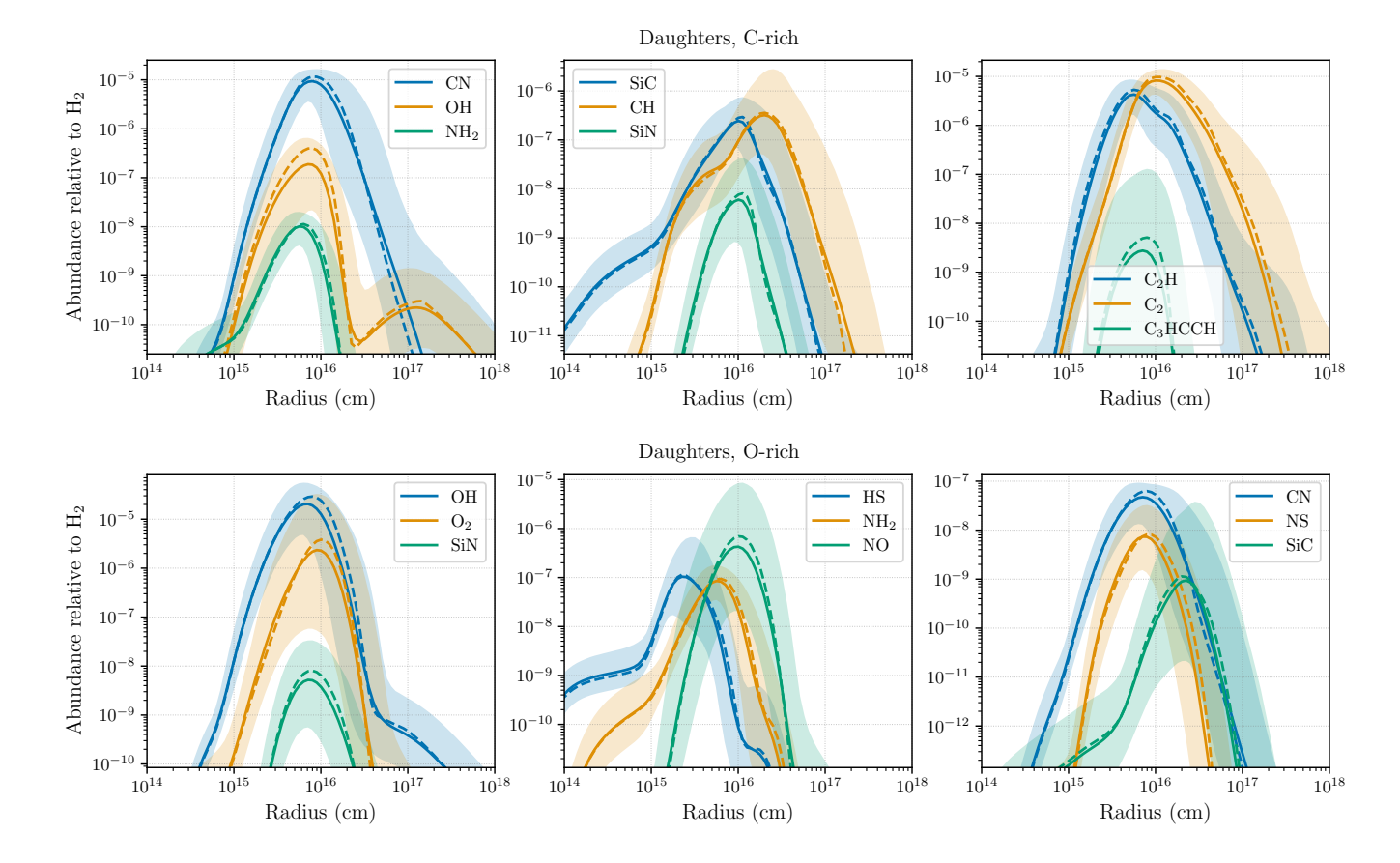


Figure 4. Fractional abundance w.r.t. H_2 of a selection of daughter species in a C-rich (top) and O-rich (bottom) outflow with $\dot{M} = 10^{-6} \, \mathrm{M}_\odot \, \mathrm{yr}^{-1}$. The dashed line shows the fiducial model prediction using RATE22. The solid line shows the mean abundance $\langle \log X(r) \rangle$ of the Monte Carlo sample of reaction networks. The shaded region contains 95.4% of all predicted profiles and corresponds to the error $\Delta \log X(r)$ on the mean abundance.

3.2.3 Mean dispersions of peak abundance and column density

Table 4 lists the mean dispersions of the peak abundance and column density and their respective standard deviations, for both groups of daughter species, where we averaged over different mass-loss rates within each group. The mean dispersion of the peak abundance is $\sim 10\%$ for both groups of daughter species, with a standard deviation of $\sim 3.5\%$ for C-rich daughters and $\sim 5\%$ for O-rich daughters. Hence, the error on the mean peak abundance is generally 10% of its value. The mean dispersion of the column density depends on the group of daughter species, where the abundant daughters have smaller values: from $\sim 11\pm 7\%$ for all C-rich daughters to $\sim 5\pm 2\%$ for the abundant, and from $\sim 14\pm 10\%$ for all O-rich daughters to $\sim 5\pm 2\%$ for the abundant. The outflow density causes only small variations in mean dispersion. The difference in dispersion on peak abundance is at most 0.5% (for abundant O-rich daughters) and on column density is at most 0.4% (for all O-rich daughters).

Fig. 7 shows scatter plots of dispersion of the peak fractional abundance versus the dispersion of the column density for the abundant daughter species for all mass-loss rates in C-rich and O-rich outflows, with the most and least uncertain daughters labelled. The most and least uncertain daughters species are summarised in Table 5. There is a clear positive correlation between the two dispersions. Species with a more precise prediction of their peak abundance hence also tend to have a more precise column density prediction. The corresponding RCCs and p-values are listed in Table D1.

4 DISCUSSION

In Sect. 4.1, we discuss the errors on the parents' envelope sizes and the impact of the error on the CO envelope size on retrieved massloss rates, and compare our model results with observations. In Sect. 4.2, we elaborate on the uncertainties on the daughter species and discuss their impact on the interpretation of observations. Finally, in Sect. 4.3, we assess the need for adding complexity to the standard chemical kinetics model, for the particular case of cyanopolyynes and hydrocarbon radicals in the outflow of IRC+10216 and in general.

4.1 Error on parents' envelope sizes

The error on the predicted envelope sizes of parent species depends on the specific molecule, the outflow's chemical composition, and, to a lesser extent, the outflow density (Fig. 3). This error is caused by chemistry, as discussed in Sect. 4.1.1. The impact of the error on the CO envelope size on retrieved mass-loss rates is discussed in Sect. 4.1.2. We compare our predicted envelope sizes to previous models and observations in Sect. 4.1.3.

4.1.1 Chemistry causing the errors on molecular envelopes

The variation in radial range of the parents' envelope sizes is not due to different errors on their photodissociation rates, as these all have accuracy *C*. Rather, it is caused by the chemistry reforming

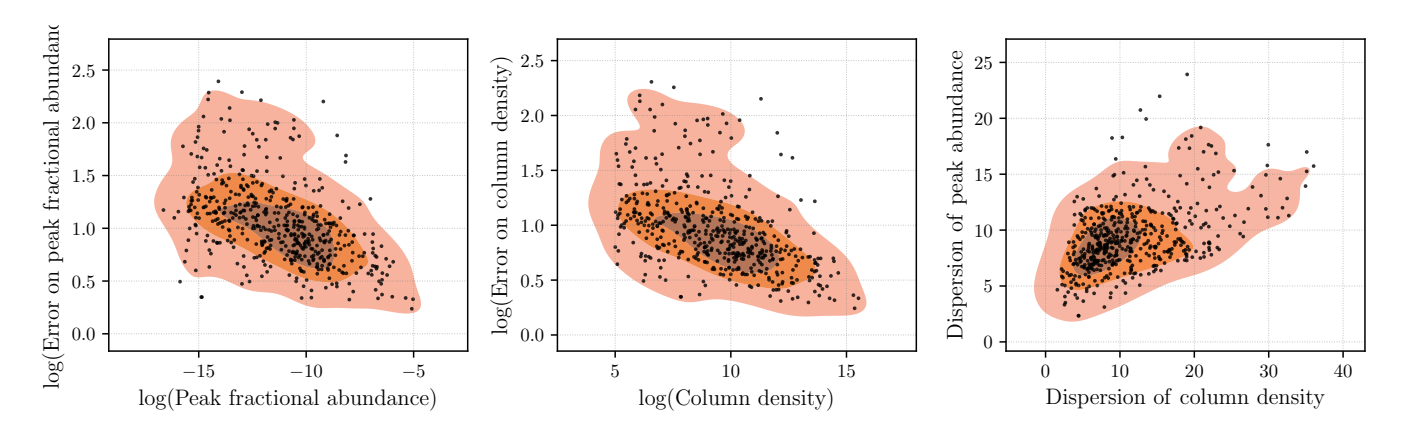


Figure 5. Scatter plots for all daughter species in a C-rich outflow with $\dot{M}=10^{-6}~\rm M_{\odot}~\rm yr^{-1}$. Left: mean peak fractional abundance versus the error on the peak abundance. Middle: mean column density versus its error. Right: dispersion of the column density versus the dispersion of the peak fractional abundance. The species have a column density of at least $10^5~\rm cm^{-2}$, removing those that do not contribute to the overall chemistry. The shaded contours show the kernel density estimation of the point distribution, with three intensity levels indicating regions of increasing point concentration.

Table 4. Mean values and standard deviations of the dispersions on peak fractional abundance and column density for the different groups of daughter species. The average is taken over the three different outflow densities for each outflow chemistry for both mean and standard deviations.

	Carbo	n-rich	Oxyge	n-rich
	All	Abun.	All	Abun.
Mean dispersion peak abundance Standard deviation	9.47% 3.02%	9.94% 3.62%	10.26% 4.56%	9.84% 4.99%
Mean dispersion column density	11.53%	5.18%	14.06%	5.17%
Standard deviation	6.65%	2.43%	9.67%	2.37%

the parent after the onset of its photodissociation. Using photodissociation models to estimate the envelope size hence might be an oversimplification.

To first order, the error on the envelope increases with the number of reactions involved in the parent's reformation. For example, the parent H_2O has a well-constrained range in radial extent and a straightforward reformation pathway: H_2O photodissociates into OH and predominantly reformed through the hydrogenation of OH.

Other parents are reformed through a more complex sequence of reactions, involving not only parents and direct photodissociation products, but also nth-generation daughter species. This is most noticeable for CS, with a radial extent of more than an order of magnitude in O-rich outflows and a factor ~5 in C-rich outflows. In C-rich outflows, CS reformation occurs via one main channel: C₂ + S, where C₂ is generated by the photodissociation of the parent SiC₂ and C₂H, a photodissociation product of the parent C₂H₂. In O-rich outflows, the main reformation pathways varies with radius. First, CS is reformed via C + HCS, the latter originating from C and the parent H₂S. Further out, the reaction between C and the parent SO takes over. Finally, the bump in abundance around 5×10^{16} cm (bottom panel, Fig. 2) is caused by the dissociative recombination of HCS⁺ with electrons. HCS⁺ arises from a sequence of reactions, ending with $H_2 + CS^+$, which in turn is produced via $S^+ + CH$. The CH radical is formed by the dissociative recombination of CH₃⁺ with electrons, itself produced by successive reactions of H₂ with C⁺.

Analysing the reaction pathways only gives us a rough sense of the general mechanism behind the origin of the error on the envelope sizes (Saltelli et al. 2019). A sensitivity analysis is needed to determine which specific reactions are the main contributors to each error. This will be done in a follow-up paper.

Table 5. Most and least precise abundant daughters species for each outflow chemistry. The most/least certain species have a dispersion of both peak abundance and column density larger/smaller than their mean plus/minus standard deviation in any outflow density.

Carbon-rich						
Most uncertain daughters	CH ₂ C ₃ N, CH, NO, SiH, HC ₄ S,					
	C_3 HCCH, C_5 N, C_4 H ₂ , C_9 H, C_5 N ⁻ ,					
	OCS, NCCN, NC ₄ N, C ₃ CCH					
Least uncertain daughters	C_6H_2 , C_4H , $HCNH^+$, NH_2 , C_2 ,					
	C ₇ H ₂ , NaCl					
(Dxygen-rich					
Most uncertain daughters	HSiS, CH, O ₂ , NO, OCS, HNSi					
Least uncertain daughters	NH ₂ , NH ₄ ⁺ , NH					

4.1.2 Impact on retrieved mass-loss rates

CO is an important density tracer for AGB outflows. Mass-loss rates are commonly determined using radiative transfer models to reproduce observed CO lines (e.g., Schöier & Olofsson 2001; Danilovich et al. 2015). Especially when using unresolved (single-dish telescope) line observations, assumptions are made about the CO envelope size. These are based on CO photodissociation and self-shielding, with Mamon et al. (1988) being the most used prescription. Saberi et al. (2019) developed a more complex model including more and updated spectroscopic data, resulting in envelope sizes up to 40% smaller than those of Mamon et al. (1988). We find that uncertainties on the chemical kinetic data cause an uncertainty on the CO envelope, which has a radial extent larger than a factor of three in all but the lowest density O-rich outflow (Fig. 3). Different CO envelope extents can impact the calculated mass-loss rates, especially when only low-energy CO lines are used in the mass-loss calculations.

To determine the impact on the retrieved mass-loss rates, we calculated radiative transfer models for the C-rich and O-rich outflows (Table 1), using the smallest and largest predicted CO envelope sizes along with the standard Mamon et al. (1988) sizes. Dust optical depths were estimated from the correlations between mass-loss rate and optical depth for the O-rich and C-rich outflows separately (Danilovich et al. 2015). Mass-loss rates were then estimated from the CO $J=2 \rightarrow 1$ and $J=1 \rightarrow 0$ line fluxes using the formula from Ramstedt et al. (2008).

For each outflow density and chemistry, we calculate a percentage difference using $(\dot{M}_{\rm max} - \dot{M}_{\rm min}) / \dot{M}_{\rm Mamon}$, where $\dot{M}_{\rm max,min}$ is the mass-

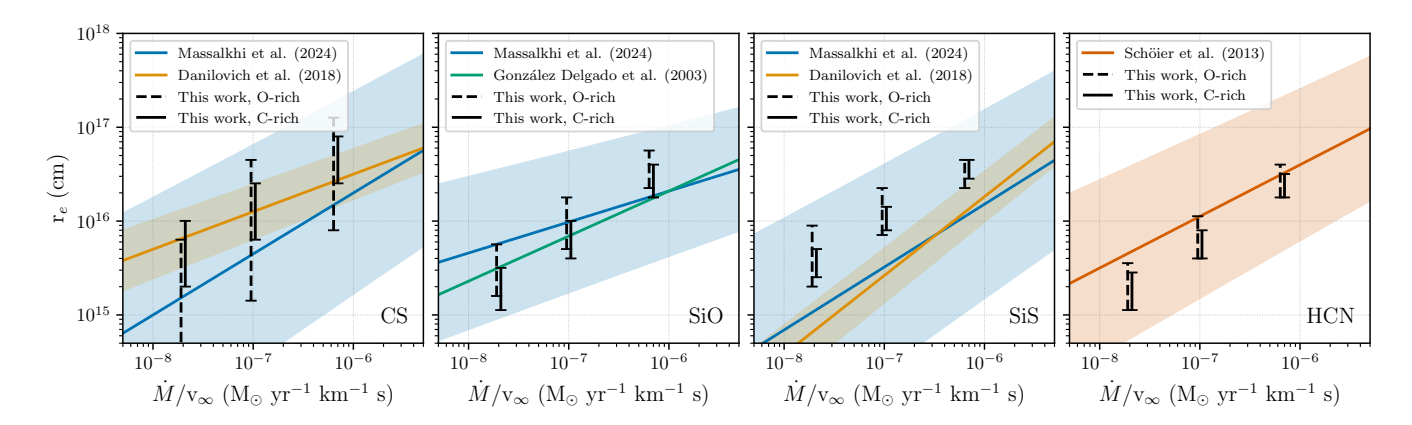


Figure 6. Variation of envelope size, r_e , with outflow density as retrieved from observations for CS, SiO, SiS, and HCN. Blue and orange: relationships and errors retrieved by Massalkhi et al. (2024) and Danilovich et al. (2018), respectively. Green: relationship retrieved by González Delgado et al. (2003), without errors. Red: relationship and error retrieved by Schöier et al. (2013). Our predicted ranges in envelope size are shown in black, for both O-rich (dashed) and C-rich (solid) outflows.

loss rates retrieved from our largest and smallest envelope sizes and $\dot{M}_{\rm Mamon}$ the mass-loss rate retrieved using Mamon et al. (1988). A similar percentage difference is calculated for the predicted line fluxes. The predicted line fluxes, mass-loss rates, and their respective percentage differences are elaborated on in Appendix E.

The CO $J=1 \rightarrow 0$ line flux uncertainty ranges from 2-155%, with a corresponding mass-loss rate uncertainty between 1.5 and 92%. We find that larger envelope sizes predict brighter low-J CO lines, as expected. The Mamon et al. (1988) envelope sizes all lie between our smallest and largest extents, but not always at the mean of our models. The CO $J=2 \rightarrow 1$ line flux uncertainty ranges from 3-58%, with corresponding mass-loss rate uncertainty between 3 and 46%. The largest differences are for the low mass-loss rate O-rich models and the smallest for the high mass-loss rate models, because the latter tend towards higher optical depths.. For all models, the relationship between change in line flux and change in apparent mass-loss rate is not a 1:1 correspondence, since excitation and optical depth effects are partially taken into account in the data the Ramstedt et al. (2008) formula was fit to.

The radial extent of the CO envelope due to chemistry is larger than the difference in envelope size between Mamon et al. (1988) and a more complex treatment of CO photodissociation (Saberi et al. 2019, factor three versus 40%), but leads to at most a factor two difference on the mass-loss rate. Therefore, the simpler Mamon et al. (1988) prescription can still be used when retrieving mass-loss rates from unresolved, low-energy CO lines.

4.1.3 Comparison to models and observations

Maes et al. (2023) determined the influence of errors on the mass-loss rate, outflow velocity, and temperature profile on the model output using the same chemical model and a reaction network based on the RATE12 network (McElroy et al. 2013). They found that the error on the predicted envelope size caused by uncertainty on outflow temperature increases with decreasing outflow density. Generally, this error is comparable to the chemical error for lower density outflows. For our high-density outflow, the chemical error is several factors larger.

The dependence of the CS, SiO, SiS, and HCN envelope sizes on outflow density has been determined observationally. Figure 6 shows the retrieved envelope size-outflow density relationships together with their error, when available, and our model predictions. The

relationships retrieved by Massalkhi et al. (2024) have an error of at least one order of magnitude for all densities; our retrieved envelope sizes lie within their errors. For CS, our models agree with the relationship retrieved by Danilovich et al. (2018) and the retrieved C-rich envelope sizes of Unnikrishnan et al. (2025). For HCN, our models agree with the relationship retrieved by Schöier et al. (2013). For SiO, our models reproduce the relationship for SiO of González Delgado et al. (2003) (without errors) relatively well, with only the high-density O-rich outflow having clearly a larger envelope size. For SiS, our model predicts larger envelope sizes than those retrieved by Danilovich et al. (2018). This was also found by Maes et al. (2023), indicating that its photodissociation rate is likely too small and lies outside its associated uncertainty range of a factor two (category C). The photodissociation cross section of SiS has never been measured or calculated. Its photodissociation rate might be similar to those of SiO and CS (van Dishoeck & Black 1988), which have unshielded rates of $\sim 10^{-9} \text{ s}^{-1}$ in the network, compared to 10^{-10} s^{-1} for SiS. For HCN, our models agree with the relationship retrieved by Schöier et al. (2013).

Photodissociation models have been used to determine the envelope sizes of species other than CO. Given that chemical reactions cause the error on the envelope size, this is an oversimplification. Maercker et al. (2008) used the prescription of Netzer & Knapp (1987) for the location of the peak in OH abundance to estimate the H₂O envelope size. We find that the Netzer & Knapp (1987) envelope sizes are slightly smaller than our predicted ranges for all outflows and chemistries. Maercker et al. (2016) retrieved the H₂O envelope size from *Herschel* observations. Their retrieved size is not well constrained, but tends to be larger than the Netzer & Knapp (1987) size for lower-density outflows The retrieved size matches the Netzer & Knapp (1987) size for the high-density outflow of IK Tau. The most H₂O transitions were detected in IK Tau's outflow, indicating that more observational data covering a variety of energies is necessary to observationally constrain envelope sizes.

4.2 Average uncertainties and model precision

The positive correlation between the dispersion of the peak fractional abundance and the dispersion of the column density of the daughter species implies that daughters with a more precise peak fractional abundance generally have a more precise column density. The av-

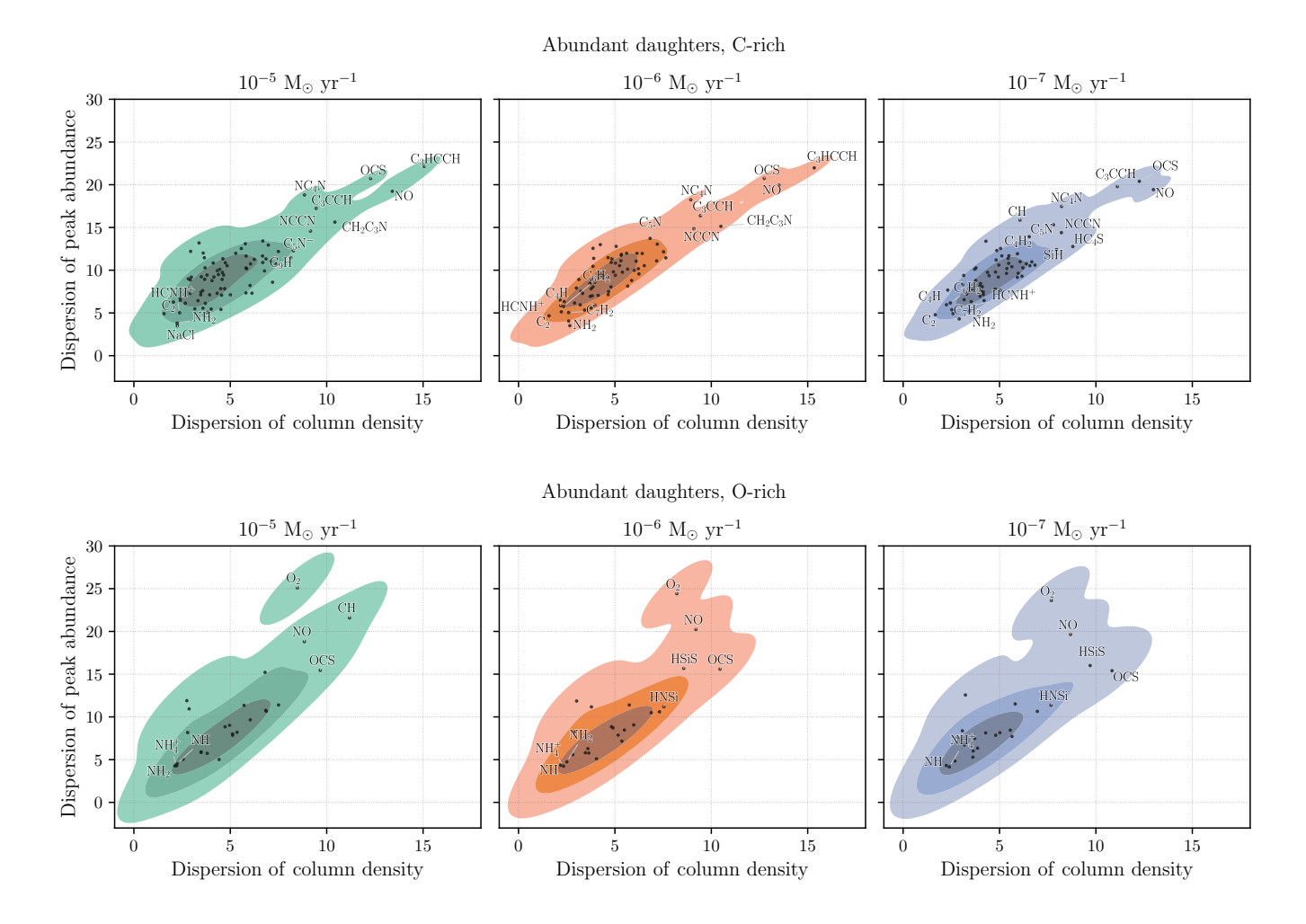


Figure 7. Scatter plots showing the dispersion of the column density versus the dispersion of the peak fractional abundance of the abundant daughter species in all C-rich (top) and O-rich (bottom) outflows. Left: outflow with $\dot{M}=10^{-5}~\rm M_{\odot}~\rm yr^{-1}$, middle: $\dot{M}=10^{-6}~\rm M_{\odot}~\rm yr^{-1}$, right: $\dot{M}=10^{-7}~\rm M_{\odot}~\rm yr^{-1}$ The shaded contours show the kernel density estimation of the point distribution, with three intensity levels indicating regions of increasing point concentration. In each panel, the top right shows the least precise daughters with a dispersion of both peak abundance and column density larger than their mean plus standard deviation (per mass-loss rate). The bottom left shows most precise daughters with dispersions smaller than their mean minus standard deviation (per mass-loss rate).

erage dispersion of the column density is smaller when considering only the abundant daughters (Table 4): the largest errors on the column density are associated with daughters with a column density below our threshold of $10^{12}~\rm cm^{-2}$. Because the higher-density inner regions contribute more to this integrated quantity, species with large uncertainties on their abundances in this region will have larger errors on their column densities.

The average uncertainties on the model predictions are discussed in Sect. 4.2.1. The radial behaviour of error on the fractional abundance profiles is addressed in Sect. 4.2.2. The impact of errors on the interpretation of observations is examined in Sect. 4.2.3.

4.2.1 Average uncertainties

The average dispersion of the peak fractional abundance is $\sim 10\%$ for all outflows and sets of daughter species. Therefore, the error on the predicted peak abundance is on average about 10% of its value. In absolute terms, this varies from a factor of a few for the most precise daughters to more than two orders of magnitude for the least precise daughters (Table 5). Interestingly, some of the most uncertain daughters are simple species, while some of the least uncertain are

longer carbon-chains. Similar to the error on the parents' envelope sizes (Sect. 4.1.1), we find that the size of the error on a predicted peak abundance is related to the number of reactions involved in the formation of the daughter species. Carbon-chains are only a few generations removed from the parent C_2H_2 in the C-rich outflow, leading to a comparatively small error on C_2 , C_4H , C_6H_2 , and C_7H_2 . On the other hand, several pathways contribute to the formation of NO, all of which require the liberation of N or O from via the photodissociation of parent species and their photoproducts. However, an uncertainty analysis does not allow us to determine the mechanisms by which the error accumulates (Saltelli et al. 2019). To determine which specific reactions are the main contributors to the error, we will perform a sensitivity analysis in a follow-up paper.

The error on the peak abundance affects the classification of HCCO as an *abundant* daughter in the highest density C-rich outflow and of CH₄ and CH₃CN in the highest density O-rich outflow. The mean peak abundances of HCCO and CH₄ drop below 10^{-12} w.r.t. H₂, but their maximum abundance is still above our threshold. The maximum peak abundance of CH₃CN increases to 15×10^{-12} w.r.t. H₂, but its mean abundance is below this threshold. None of the most precise species are first-generation daughter species (C₂ is mostly produced

by the photodissociation of C_2H and not by photodissociation of the C-rich parent SiC_2). This indicates that the error on the model predictions is highly dependent on the reactions forming and destroying each species.

4.2.2 Non-propagation of errors

We find that errors on predicted abundances do not propagate throughout the outflow, but fluctuate locally without systematic accumulation. The error on the daughter abundance profiles and the radial spread on the parents' abundance profiles does not necessarily grow with increasing radius.

This is due to the nature of our chemical system. The dominant chemical processes change throughout the outflow in response to its gradient in density and temperature, effectively generating a new set of ordinary differential equations at each radius. Consequently, the error on the predicted abundance of a species reflects how well the model captures the dominant chemical processes of that species at a particular location within the outflow, rather than being accumulated from previous computational steps.

4.2.3 Impact on the interpretation of observations

Given the average dispersion of $\sim 10\%$ on the predicted peak abundance, caution is needed when fitting predicted (peak) abundances to abundances retrieved from observations. Ad hoc modifications to the physics or chemistry of a model should generally be avoided, especially for the least certain species (Table 5). While these could explain away disagreement with observations, it might not to so in a meaningful way as the "improved" prediction could still lie within the (unquantified) uncertainty of the fiducial model.

Caution is especially needed when retrieving or refining reaction rates based on observations, as the error on the retrieved abundances is generally not taken into account. The improved agreement could therefore lie within the (unquantified) error of the chemical model and/or the (unquantified) error of the retrieved abundance.

4.3 Assessing the need for added complexity

Observations have driven the development of the standard CSE model, as gas-phase only chemistry in a smooth outflow does not always reproduce retrieved abundance profiles. This uncertainty analysis allows us to address which discrepancies with observations can be solved by an increase in complexity of the model. Our criteria are based on differences between predicted and retrieved abundances and the general behaviour of the abundance profile.

In Sect. 4.3.1, we discuss the need for tailoring a chemical model to the outflow of the C-rich AGB star IRC +10216 to describe the observed radial distribution of cyanopolyynes and hydrocarbons. Sect. 4.3.2 examines the general need for dust-gas chemistry, porosity, and the UV field of a close-by stellar companion.

4.3.1 Cyanopolyynes and hydrocarbons around IRC+10216

Chemical models have been specifically tailored to the outflow of the C-rich AGB star IRC+10216, which contains multiple broken shell-like structures (e.g., Mauron & Huggins 2006; De Beck et al. 2012; Cernicharo et al. 2015). Although IRC+10216 is the most studied AGB outflow, the distribution of cyanopolyynes (HC_{2n+1}N, n = 3, 5, 7, ...) and hydrocarbon radicals (C_{2n}H, n = 1, 2, 3, ...) in its outer regions is a long-standing puzzle. Standard chemical

models predict a radial sequence with molecule length. While the cyanopolyynes show such a radial sequence, the hydrocarbon radicals are cospatial (Guélin et al. 1999; Agúndez et al. 2017; Keller 2017). To solve these discrepancies, density-enhanced dust shells have been included (Brown & Millar 2003; Cordiner & Millar 2009) and the extinction throughout the inhomogeneous outflow has been lowered (Agúndez et al. 2017). Despite these efforts, the different spatial behaviour of these molecules remains unexplained.

Figure 8 shows the fractional abundances of cyanopolyynes and hydrocarbons in the C-rich outflow with $\dot{M}=10^{-5}~\rm M_{\odot}~\rm yr^{-1}$, which is closest in outflow density to IRC +10216. From the mean abundance profiles, we find a radial sequence of the cyanopolyynes and cospatial hydrocarbons, in agreement with observations. However, uncertainties on the chemical kinetic data also lead to a radial spread of the peak abundances; $\rm C_6H$ and $\rm C_6H^-$ are particularly ill-constrained. To better compare to Figure 6 of Agúndez et al. (2017), Figure 9 shows the predicted number densities of these molecules, with radius converted to arcsec using a distance to IRC +10216 of 123 pc (Groenewegen et al. 2012). We find that CN and $\rm C_3N$ peak at the same radius, as observed and unlike the model predictions of Agúndez et al. (2017).

Within the uncertainties on the chemical kinetic data, the classic spherically symmetric outflow model is hence able to reproduce the observed cospatial distribution of the cyanopolyynes and hydrocarbons. This implies that the effects of the observed density distributions are smaller than those caused by the uncertainties on the kinetic data. Therefore, adding physical or chemical complexity to the standard model does not aid in the interpretation of the relative locations of these molecules.

4.3.2 Dust-gas chemistry, porosity, and companion UV radiation

Dust-gas chemistry was included (Van de Sande et al. 2019, 2020, 2021) to assess whether it could indeed lead to a decrease in abundance of SiO and SiS before their photodissociation, as observed in high density O-rich outflows (e.g. Bujarrabal et al. 1989; Decin et al. 2010; Verbena et al. 2019). Further clues for gas-phase depletion onto dust grains are found in trends in abundance with outflow density, where the abundance of SiO, SiS, and CS with is found to decrease with increasing outflow density (e.g., González Delgado et al. 2003; Massalkhi et al. 2019; Danilovich et al. 2019; Massalkhi et al. 2024).

Uncertainties on the chemical kinetic data cannot reproduce the observed abundance profiles of SiO and SiS; the uncertainty on their envelope sizes does not extend into the region in the intermediate wind where SiO and SiS are observed to decrease (Decin et al. 2010). Including dust-gas chemistry is hence necessary to close the gap with observations, especially for higher-density outflows: Van de Sande et al. (2019) included a comprehensive dust-gas chemistry and was able to reproduce the observed depletion of SiO and SiS. Additionally, H₂O ice is observed around OH/IR stars Sylvester et al. (1999). Dust-gas chemistry, either simple (e.g. Jura & Morris 1985; Dijkstra et al. 2003) or complex (Van de Sande et al. 2019, 2020), is necessary include the formation of ices and refractory organics (Van de Sande et al. 2021) on grain surfaces.

The porosity formalism can be used to approximate non-spherically symmetric outflows (Van de Sande et al. 2018). A porous outflow does not significantly impact the composition of the outflow and mostly affects the radial extent of species. It can enhance the influence of the UV field of a close-by stellar companion. This can increase the chemical complexity of the inner wind (Van de Sande & Millar 2022). This includes the species SiN, SiC, and NS, which were observed to have large abundances in the inner region of W Aql's outflow (Danilovich et al. 2024), which is shaped by binary inter-

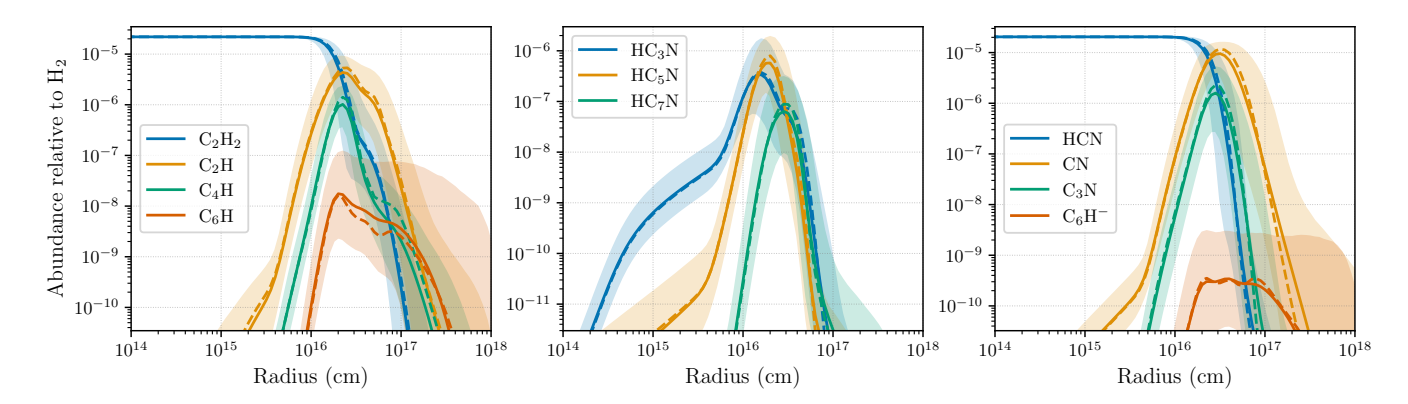


Figure 8. Fractional abundance w.r.t. H_2 of selected carbon chains in a C-rich outflow with $\dot{M} = 10^{-5} \text{ M}_{\odot} \text{ yr}^{-1}$. The dashed line shows the fiducial model prediction using RATE22. The solid line shows the mean abundance $\langle \log X(r) \rangle$ of the Monte Carlo sample of reaction networks. The shaded region contains 95.4% of all predicted profiles and corresponds to the error $\Delta \log X(r)$ on the mean abundance.

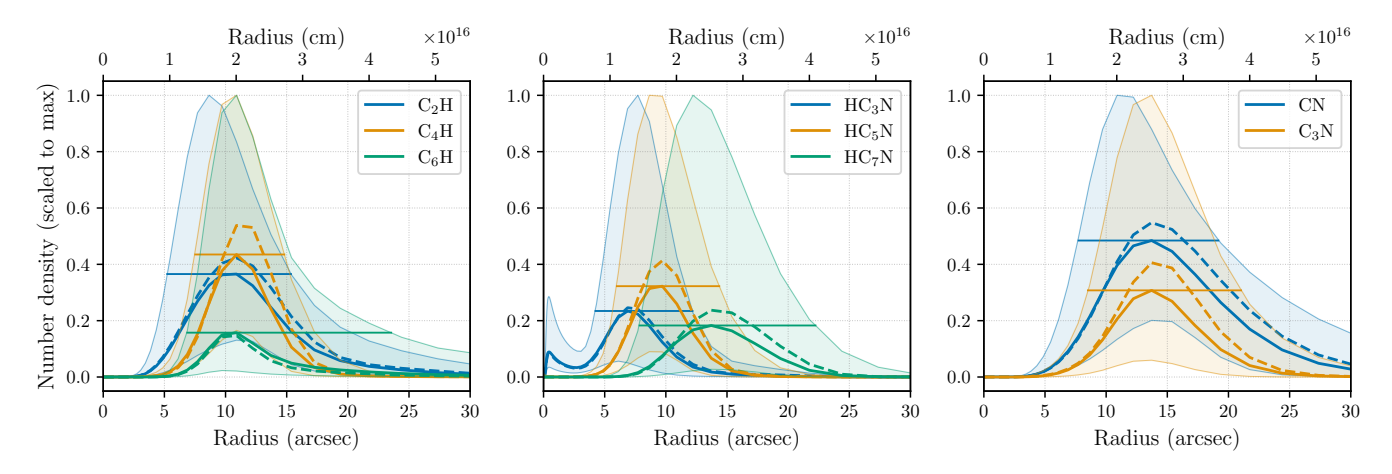


Figure 9. Number density scaled to the mean peak value of selected carbon chains in a C-rich outflow with $\dot{M}=10^{-5}~\rm M_{\odot}~\rm yr^{-1}$. Radius in arcsec assumes a distance of 123 pc (the distance to IRC+10216, Groenewegen et al. 2012). The dashed line shows the fiducial model prediction using RATE22. The solid line shows the mean abundance $\langle \log X(r) \rangle$ of the Monte Carlo sample of reaction networks. The shaded region contains 95.4% of all predicted profiles and corresponds to the error $\Delta \log X(r)$ on the mean abundance. The horizontal line shows the range where the abundance is at least the mean peak abundance.

action (e.g., Ramstedt et al. 2017). Uncertainties on the kinetic data cannot account for their large observed abundances and asymmetric distributions in the intermediate outflow. Including the effects of its known F9 companion is essential to do so.

 HC_3N is observed to have an unexpectedly large abundance in IRC+10216's inner wind Siebert et al. (2022). Including a solar-like companion and porosity increased its predicted abundance by an order of magnitude. Additionally, different parent abundances affects the HC_3N abundance in the inner wind. The initial C_2H_2 and HCN abundances used in the chemical model presented in Siebert et al. (2022) are a factor two lower than those used here to ensure agreement with observational results of Fonfría et al. (2008). This leads to an HC_3N abundance about one order of magnitude smaller than the abundance shown in Fig. 8.

A porous outflow, especially combined with a stellar companion, can increase the SO and SO₂ abundance before their photodissociation. This is observed for higher density O-rich outflows (Danilovich et al. 2016, 2020). Uncertainty on the kinetic data allows for rates that would increase their abundance before photodissociation, but only by a factor of a few (Fig. 2). This is linked to the uncertainty on the H₂O envelope. The increases predicted by our model are smaller than those observed, added chemical complexity is hence necessary

to interpret the SO and SO₂ observations. We note that SiS also allows for an increase in abundance before photodissociation in O-rich outflows (bottom panel, Fig. 2); this has not been observed so far.

5 CONCLUSIONS

We presented the first uncertainty analysis of the standard CSE model, where we quantify the effect of uncertainties in the chemical kinetic data on the model output, for both C-rich and O-rich outflows at different outflow densities. This is also the first such analysis of the RATE22 reaction network. We used a Monte Carlo sampling method to propagate the uncertainties, generating 10,000 reaction networks, and assessed their effects on the fractional abundance and column density predictions, quantifying their mean values and errors.

Uncertainties on the chemical kinetic data lead to errors on the size of the parents' molecular envelope. The size of the error is not due to the uncertainty on their photodissociation rates, as these are all a factor of two for the relevant reactions, but rather due to the chemistry reforming the parent after its photodissociation. Therefore, using photodissociation models to constrain envelope sizes might be an oversimplification. In particular, the error on the CO envelope is

larger than the improvement on its size achieved when using more complex photodissociation models. Although the CO envelope is not well constrained, its error only affects the retrieved mass-loss rates by at most a factor of two.

The error on the fractional abundance does not propagate throughout the outflow. The non-accumulation of errors is due to the nature of the outflow, as the gradients in temperature and density set the main chemical processes throughout the outflow. Hence, it is a reflection of how well the model captures the chemistry of each species at each radius. For the daughter species, we find that the dispersion of the peak fractional abundance is correlated with that of the column density. Species with a more precise peak fractional abundance estimate hence tend to have a more precise column density estimate. The average dispersion is about 10% for the peak fractional abundance and 5% for the column density. This leads us to caution against refining or deriving rate coefficients from observations of CSEs.

The standard CSE model of gas-phase chemistry in a smooth outflow is still widely applicable to observations. For example, the radial distribution of the cyanopolyynes and hydrocarbon radicals around IRC+10216 can be reproduced without adding complexity to the standard model of gas-phase chemistry in a smooth outflow, despite observed density structure, as uncertainties in the kinetic data dominate over these structures. Including complexities as spherical asymmetries, dust-gas chemistry, and/or the UV field of a close-by stellar companion, is only necessary to explain certain observations. These include gas-phase depletion onto dust grains and photo-induced chemical complexity taking place in the inner regions.

Our uncertainty analysis only characterises the uncertainty in the model predictions due to the uncertainty on the input chemical kinetic data. To determine which reactions contribute the most to the uncertainty on the model predictions, we will perform a sensitivity analysis in a follow-up paper.

ACKNOWLEDGEMENTS

MVdS acknowledges support from the European Union's Horizon 2020 research and innovation programme under the Marie Skłodowska-Curie grant agreement No 882991 and the Oort Fellowship at Leiden Observatory, and thanks the Munich Institute for Astro-, Particle and BioPhysics (MIAPbP), which is funded by the Deutsche Forschungsgemeinschaft (DFG, German Research Foundation) under Germany's Excellence Strategy – EXC-2094 – 390783311, for fostering insightful discussions. MG acknowledges support from the European Union's Horizon 2020 research and innovation programme under the Marie Skłodowska-Curie grant agreement No 101026214. TJM gratefully acknowledges the STFC for support under grant reference ST/T000198/1. TD is supported in part by the Australian Research Council through a Discovery Early Career Researcher Award (DE230100183).

DATA AVAILABILITY

The data underlying this article will be shared on reasonable request to the corresponding author.

REFERENCES

Agúndez M., Cernicharo J., 2006, ApJ, 650, 374 Agúndez M., Cernicharo J., Guélin M., 2010, ApJ, 724, L133 Agúndez M., et al., 2017, A&A, 601, A4 Agúndez M., Martínez J. I., de Andres P. L., Cernicharo J., Martín-Gago J. A., 2020, A&A, 637, A59

Bensberg M., Reiher M., 2024, The Journal of Physical Chemistry A, 128, 4532

Brown J. M., Millar T. J., 2003, MNRAS, 339, 1041

Bujarrabal V., Gomez-Gonzalez J., Planesas P., 1989, A&A, 219, 256

Cernicharo J., Marcelino N., Agúndez M., Guélin M., 2015, A&A, 575, A91 Charnley S. B., Smith R. G., 1993, in Weinberger R., Acker A., eds, IAU

Symposium Vol. 155, Planetary Nebulae. p. 329

Cherchneff I., Glassgold A. E., 1993, ApJ, 419, L41

Cordiner M. A., Millar T. J., 2009, ApJ, 697, 68

Danilovich T., et al., 2015, A&A, 581, A60

Danilovich T., De Beck E., Black J. H., Olofsson H., Justtanont K., 2016, A&A, 588, A119

Danilovich T., Van de Sande M., De Beck E., Decin L., Olofsson H., Ramstedt S., Millar T. J., 2017, A&A, 606, A124

Danilovich T., Ramstedt S., Gobrecht D., Decin L., De Beck E., Olofsson H., 2018, A&A, 617, A132

Danilovich T., Richards A. M. S., Karakas A. I., Van de Sande M., Decin L., De Ceuster F., 2019, MNRAS, 484, 494

Danilovich T., Richards A. M. S., Decin L., Van de Sande M., Gottlieb C. A., 2020, MNRAS, 494, 1323

Danilovich T., et al., 2024, Nature Astronomy, 8, 308

De Beck E., et al., 2012, A&A, 539, A108

Decin L., 2021, ARA&A, 59, 337

Decin L., et al., 2010, Nature, 467, 64

Decin L., et al., 2020, Science, 369, 1497

Dijkstra C., Dominik C., Hoogzaad S. N., de Koter A., Min M., 2003, A&A, 401, 599

Dijkstra C., Dominik C., Bouwman J., de Koter A., 2006, A&A, 449, 1101

Dobrijevic M., Parisot J. P., 1998, Planet. Space Sci., 46, 491

Dobrijevic M., Ollivier J. L., Billebaud F., Brillet J., Parisot J. P., 2003, A&A, 398, 335

Dobrijevic M., Hébrard E., Plessis S., Carrasco N., Pernot P., Bruno-Claeys M., 2010, Advances in Space Research, 45, 77

Draine B. T., 1978, ApJS, 36, 595

Fonfría J. P., Cernicharo J., Richter M. J., Lacy J. H., 2008, ApJ, 673, 445

Goldreich P., Scoville N., 1976, ApJ, 205, 144

González Delgado D., Olofsson H., Kerschbaum F., Schöier F. L., Lindqvist M., Groenewegen M. A. T., 2003, A&A, 411, 123

Groenewegen M. A. T., et al., 2012, A&A, 543, L8

Guélin M., Neininger N., Lucas R., Cernicharo J., 1999, in Ossenkopf V., Stutzki J., Winnewisser G., eds, The Physics and Chemistry of the Interstellar Medium.

Homan W., Danilovich T., Decin L., de Koter A., Nuth J., Van de Sande M., 2018, A&A, 614, A113

Huggins P. J., Glassgold A. E., 1982, ApJ, 252, 201

Jura M., Morris M., 1985, ApJ, 292, 487

Keller D., 2017, PhD thesis, Rheinische Friedrich Wilhelms University of Bonn, Germany

Kervella P., Homan W., Richards A. M. S., Decin L., McDonald I., Montargès M., Ohnaka K., 2016, A&A, 596, A92

Khouri T., et al., 2016, A&A, 591, A70

Li X., Millar T. J., Heays A. N., Walsh C., van Dishoeck E. F., Cherchneff I., 2016, A&A, 588, A4

Maercker M., Schöier F. L., Olofsson H., Bergman P., Ramstedt S., 2008, A&A, 479, 779

Maercker M., Danilovich T., Olofsson H., De Beck E., Justtanont K., Lombaert R., Royer P., 2016, A&A, 591, A44

Maes S., Van de Sande M., Danilovich T., De Ceuster F., Decin L., 2023, MNRAS, 522, 4654

Mamon G. A., Glassgold A. E., Huggins P. J., 1988, ApJ, 328, 797

Massalkhi S., Agúndez M., Cernicharo J., 2019, A&A, 628, A62

Massalkhi S., Agúndez M., Cernicharo J., Velilla-Prieto L., 2020, A&A, 641, A57

Massalkhi S., Agúndez M., Fonfría J. P., Pardo J. R., Velilla-Prieto L., Cernicharo J., 2024, A&A, 688, A16

Mauron N., Huggins P. J., 2006, A&A, 452, 257

```
McElroy D., Walsh C., Markwick A. J., Cordiner M. A., Smith K., Millar
    T. J., 2013, A&A, 550, A36
Millar T. J., Herbst E., 1994, A&A, 288, 561
Millar T. J., Herbst E., Bettens R. P. A., 2000, MNRAS, 316, 195
Millar T. J., Walsh C., Van de Sande M., Markwick A. J., 2024, A&A, 682,
Morris M. D., 1991, Technometrics, 33, 161
Morris M., Jura M., 1983, ApJ, 264, 546
Nejad L. A. M., Millar T. J., Freeman A., 1984, A&A, 134, 129
Netzer N., Knapp G. R., 1987, ApJ, 323, 734
Penteado E. M., Walsh C., Cuppen H. M., 2017, ApJ, 844, 71
Ramstedt S., Schöier F. L., Olofsson H., Lundgren A. A., 2008, A&A, 487,
    645
Ramstedt S., et al., 2017, A&A, 605, A126
Saberi M., Vlemmings W. H. T., De Beck E., 2019, A&A, 625, A81
Safonov B. S., Zheltoukhov S. G., Tatarnikov A. M., Strakhov I. A., Shenavrin
    V. I., 2025, AJ, 169, 140
Saltelli A., Aleksankina K., Becker W., Fennell P., Ferretti F., Holst N., Li S.,
    Wu Q., 2019, Environmental Modelling & Software, 114, 29
Scalo J. M., Slavsky D. B., 1980, ApJ, 239, L73
Schöier F. L., Olofsson H., 2001, A&A, 368, 969
Schöier F. L., Ramstedt S., Olofsson H., Lindqvist M., Bieging J. H., Marvel
    K. B., 2013, A&A, 550, A78
Siebert M. A., Van de Sande M., Millar T. J., Remijan A. J., 2022, Astrophys.
    J. 941.90
Stewart R. W., Thompson A. M., 1996, J. Geophys. Res., 101, 20,953
Sylvester R. J., Kemper F., Barlow M. J., de Jong T., Waters L. B. F. M.,
    Tielens A. G. G. M., Omont A., 1999, A&A, 352, 587
Teyssier D., Hernandez R., Bujarrabal V., Yoshida H., Phillips T. G., 2006,
    A&A, 450, 167
Thompson A. M., Stewart R. W., 1991, J. Geophys. Res., 96, 13,089
Unnikrishnan R., et al., 2025, A&A, 699, A48
Van de Sande M., Millar T. J., 2022, Mon. Not. R. Astron. Soc., 510, 1204
Van de Sande M., Sundqvist J. O., Millar T. J., Keller D., Homan W., de Koter
    A., Decin L., De Ceuster F., 2018, A&A, 616, A106
Van de Sande M., Walsh C., Mangan T. P., Decin L., 2019, Mon. Not. R.
    Astron. Soc., p. 2325
Van de Sande M., Walsh C., Danilovich T., 2020, Mon. Not. R. Astron. Soc.,
Van de Sande M., Walsh C., Millar T. J., 2021, Mon. Not. R. Astron. Soc.,
Van de Sande M., Walsh C., Millar T. J., 2023, Faraday Discussions, 245, 586
Vasyunin A. I., Sobolev A. M., Wiebe D. S., Semenov D. A., 2004, Astronomy
    Letters, 30, 566
Vasyunin A. I., Semenov D., Henning T., Wakelam V., Herbst E., Sobolev
```

Verbena J. L., Bujarrabal V., Alcolea J., Gómez-Garrido M., Castro-Carrizo

Wakelam V., Selsis F., Herbst E., Caselli P., 2005, A&A, 444, 883 Wakelam V., Herbst E., Selsis F., 2006a, A&A, 451, 551

Wakelam V., Herbst E., Selsis F., Massacrier G., 2006b, A&A, 459, 813 Wakelam V., Herbst E., Le Bourlot J., Hersant F., Selsis F., Guilloteau S.,

van Dishoeck E. F., Black J. H., 1988, in Millar T. J., Williams D. A., eds, Astrophysics and Space Science Library Vol. 146, Rate Coefficients in

Astrochemistry. p. 209, doi:10.1007/978-94-009-3007-0_15

APPENDIX A: DEVIATIONS FROM A LOGNORMAL DISTRIBUTION

Fig. A1 illustrates the deviation from a Gaussian distribution of the logarithm of the predicted fractional abundances. Rapid changes in abundance, caused by e.g., the onset of photodissociation, lead to a non-Gaussian distribution of $\log X$ (Wakelam et al. 2005). Using the standard deviation as a measure of the error is in these cases not appropriate. We therefore use the smallest interval that contains 95.4% of all abundance profiles (Eq. 3) to determine the error.

Similarly, Fig. A2 illustrates how the logarithm of the predicted column densities can also deviate from a Gaussian distribution. For most species, the smallest interval that contains 95.4% of all column densities corresponds to 2 times the standard deviation. This is not the case for species with a non-lognormal distribution of their predicted column densities (bottom panel).

APPENDIX B: CONVERGENCE OF THE MONTE CARLO SAMPLING METHOD

To determine the convergence of the Monte Carlo sampling method results, we assessed the stability of our predictions with increasing sample size. Convergence was deemed adequate if increasing the sample size does not produce significant changes in the final predictions. Specifically, we evaluated the relative change in the mean and error of the column densities and peak fractional abundances as the sample size increases. The predictions were calculated for increasing sample sizes, using increments of 200.

For all outflow chemistries and densities, we find that the relative change in all estimates with increasing the sample size lies well below 1%. The convergence of the Monte Carlo modelling is illustrated in Fig. B1, which shows the convergence trajectories of the mean column densities and their dispersions normalised to their final values for all daughter species in the C-rich outflow with $10^{-6}~M_{\odot}~yr^{-1}$. These convergence trajectories for the column density and its dispersion and the peak fractional abundance and its error for all outflow chemistries and densities. Our sample size of 10,000 models is therefore sufficient.

A. M., 2008, ApJ, 672, 629 Velilla-Prieto L., et al., 2023, Nature, 617, 696

A., 2019, A&A, 624, A107

2010, A&A, 517, A21

Wittkowski M., et al., 2017, A&A, 601, A3

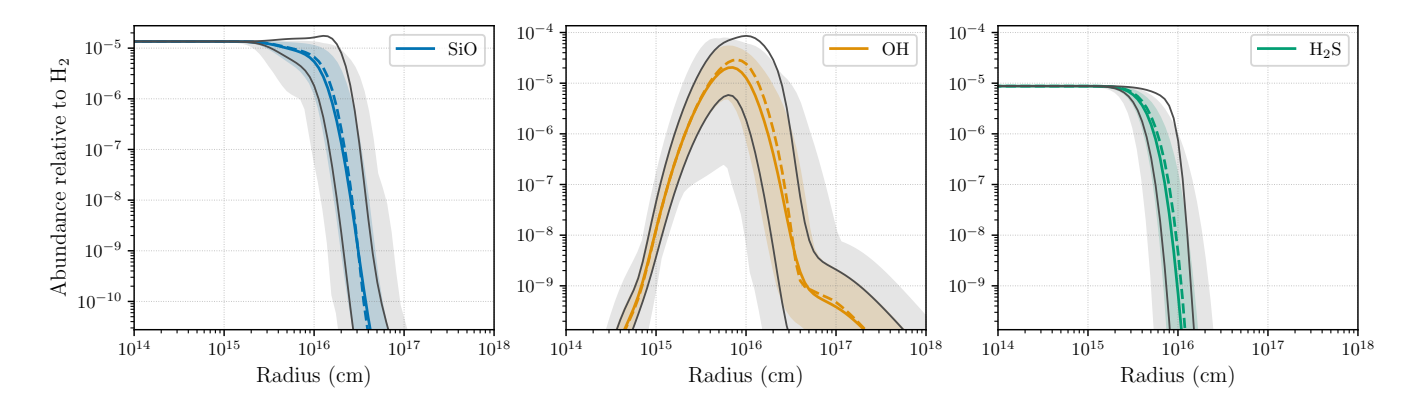


Figure A1. Fractional abundance w.r.t. H_2 of SiO, OH, and H_2 S in the O-rich outflow with $\dot{M}=10^{-6}~\rm M_\odot~\rm yr^{-1}$. The dashed coloured line shows the fiducial model prediction using RATE22. The solid coloured line shows the mean abundance $\langle \log X(r) \rangle$ of the Monte Carlo sample of reaction networks. The coloured shaded region contains 95.4% of all predicted profiles and corresponds to the error $\Delta \log X(r)$ on the mean abundance. The grey shaded region contains all 10,000 predicted profiles. The black lines show the mean abundance $\pm 2 \times$ the standard deviation of the distribution of $\log X$.

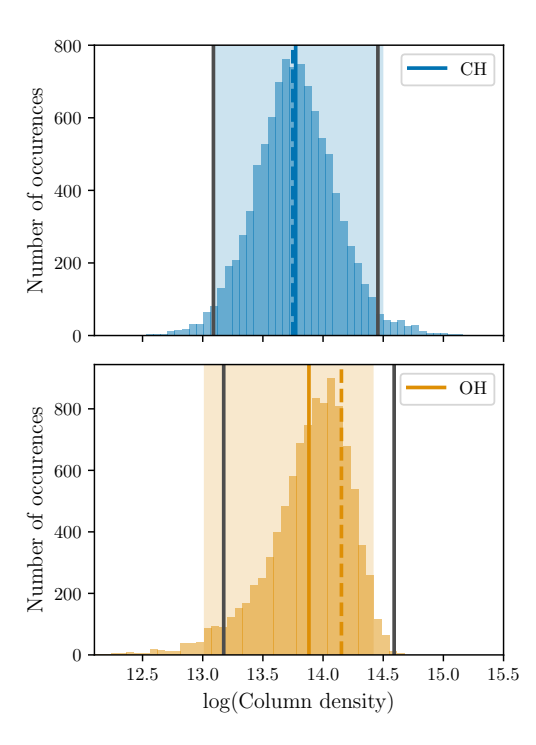


Figure A2. Histogram of the predicted column densities of CH and OH in the C-rich outflow with $\dot{M}=10^{-6}~M_{\odot}~yr^{-1}$. The dashed coloured line shows the fiducial model prediction using RATE22. The solid coloured line shows the mean column density of the Monte Carlo sample of reaction networks. The shaded region contains 95.4% of all predicted profiles and corresponds to the error on the column density. The black lines show the mean column density $\pm~2\times$ the standard deviation of the distribution of predicted column densities.

APPENDIX C: RADIAL EXTENT PARENTS

Table C1 lists the radial extent of the molecular envelopes of the parent species in C-rich and O-rich outflows. These are shown in Fig. 3. The mean radial extent is given along with the smallest and largest predicted values.

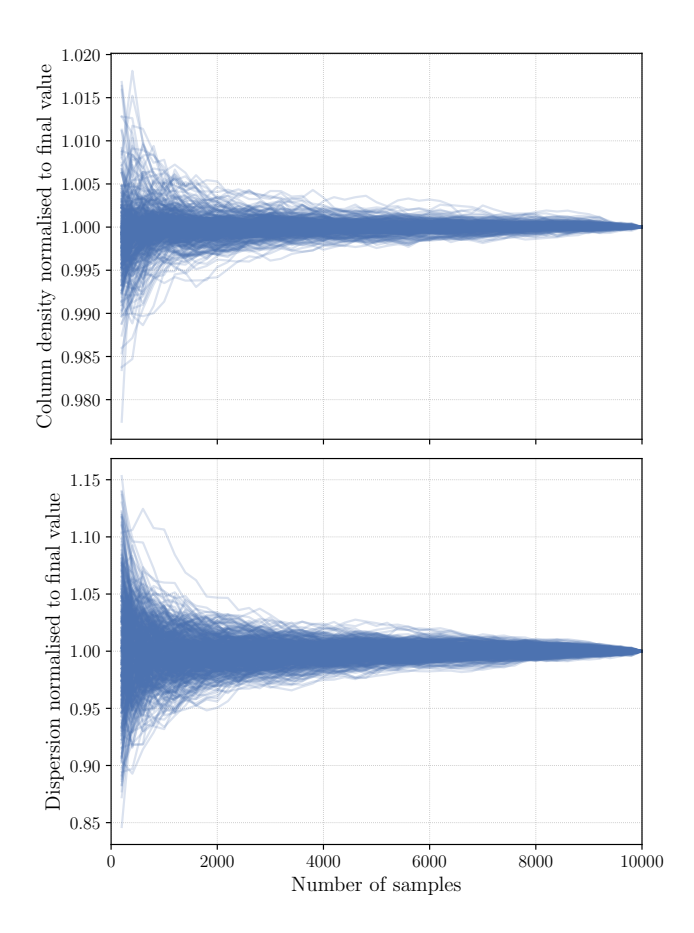


Figure B1. Convergence trajectories for (top) column density and (bottom) its dispersion for all daughter species in the C-rich outflow with $10^{-6} \text{ M}_{\odot} \text{ yr}^{-1}$. The predictions are calculated for increasing sample sizes, using increments of 200, and normalised to their final values.

APPENDIX D: DISPERSION ALL DAUGHTERS

Table D1 lists the Spearman rank correlation coefficients between the mean peak fractional abundance and its error, the mean column density and its error, and the dispersion of the column density and the dispersion of the peak fractional abundance for all daughters and

Table C1. Radial extent of the molecular envelopes of the parent species in C-rich (*top*) and O-rich (*bottom*) outflows for different mass-loss rates. For each mass-loss rate, the mean radial extent of the molecular envelope is listed, along with the smallest and largest predicted values (min and max, respectively). All values are in cm.

	Carbon-rich									
		$10^{-5}~M_{\odot}~yr^{-1}$			$10^{-6}~M_{\odot}~yr^{-1}$			$10^{-7} \ {\rm M}_{\odot} \ {\rm yr}^{-1}$		
Species	Min	Mean	Max	Min	Mean	Max	Min	Mean	Max	
CO	1.79×10^{17}	2.25×10^{17}	5.65×10^{17}	5.65×10^{16}	7.98×10^{16}	2.00×10^{17}	2.52×10^{16}	3.56×10^{16}	8.96×10^{16}	
N_2	4.00×10^{16}	6.34×10^{16}	1.27×10^{17}	1.13×10^{16}	1.79×10^{16}	5.04×10^{16}	3.57×10^{15}	6.34×10^{15}	2.00×10^{16}	
H_2O	2.00×10^{16}	2.83×10^{16}	3.56×10^{16}	5.04×10^{15}	7.11×10^{15}	1.13×10^{16}	1.27×10^{15}	2.00×10^{15}	3.18×10^{15}	
HCN	1.79×10^{16}	2.25×10^{16}	3.18×10^{16}	4.00×10^{15}	5.65×10^{15}	7.98×10^{15}	1.13×10^{15}	1.59×10^{15}	2.83×10^{15}	
NH_3	1.59×10^{16}	1.79×10^{16}	2.25×10^{16}	4.00×10^{15}	5.04×10^{15}	6.34×10^{15}	1.13×10^{15}	1.42×10^{15}	2.00×10^{15}	
H_2S	1.59×10^{16}	2.00×10^{16}	2.52×10^{16}	3.18×10^{15}	4.49×10^{15}	5.65×10^{15}	7.98×10^{14}	1.13×10^{15}	1.42×10^{15}	
SiO	1.79×10^{16}	2.52×10^{16}	4.00×10^{16}	4.00×10^{15}	5.65×10^{15}	1.01×10^{16}	1.13×10^{15}	1.59×10^{15}	3.18×10^{15}	
SiS	2.83×10^{16}	3.56×10^{16}	4.49×10^{16}	7.98×10^{15}	1.01×10^{16}	1.42×10^{16}	2.52×10^{15}	3.18×10^{15}	5.04×10^{15}	
CS	2.52×10^{16}	4.49×10^{16}	7.98×10^{16}	6.34×10^{15}	1.13×10^{16}	2.52×10^{16}	2.00×10^{15}	4.00×10^{15}	1.01×10^{16}	
HCl	1.79×10^{16}	2.25×10^{16}	3.56×10^{16}	4.00×10^{15}	5.65×10^{15}	1.01×10^{16}	1.01×10^{15}	1.59×10^{15}	3.18×10^{15}	
HF	3.18×10^{16}	4.00×10^{16}	5.04×10^{16}	8.96×10^{15}	1.13×10^{16}	1.59×10^{16}	4.00×10^{15}	5.04×10^{15}	7.11×10^{15}	
CH_4	2.00×10^{16}	2.52×10^{16}	3.18×10^{16}	4.49×10^{15}	5.65×10^{15}	8.96×10^{15}	1.13×10^{15}	1.79×10^{15}	2.83×10^{15}	
C_2H_2	1.42×10^{16}	1.79×10^{16}	2.25×10^{16}	3.18×10^{15}	4.00×10^{15}	5.65×10^{15}	8.96×10^{14}	1.27×10^{15}	2.00×10^{15}	
C_2H_4	1.42×10^{16}	1.79×10^{16}	2.52×10^{16}	3.18×10^{15}	4.00×10^{15}	5.04×10^{15}	7.98×10^{14}	1.01×10^{15}	1.42×10^{15}	
SiC_2	3.18×10^{16}	4.00×10^{16}	5.65×10^{16}	7.98×10^{15}	1.13×10^{16}	2.00×10^{16}	2.52×10^{15}	4.00×10^{15}	7.11×10^{15}	
HCP	2.00×10^{16}	2.83×10^{16}	5.04×10^{16}	5.04×10^{15}	7.98×10^{15}	1.59×10^{16}	1.42×10^{15}	2.52×10^{15}	5.65×10^{15}	

Oxygen-	

		$10^{-5}\ M_{\odot}\ yr^{-1}$		$10^{-6}~{ m M}_{\odot}~{ m yr}^{-1}$				$10^{-7} \ { m M}_{\odot} \ { m yr}^{-1}$			
Species	Min	Mean	Max	Min	Mean	Max		Min	Mean	Max	
CO	1.27×10^{17}	1.59×10^{17}	3.56×10^{17}	4.00×10^{16}	5.65×10^{16}	1.27×10^{17}		1.59×10^{16}	2.25×10^{16}	5.65×10^{16}	
N_2	4.00×10^{16}	5.65×10^{16}	1.27×10^{17}	1.01×10^{16}	1.79×10^{16}	4.49×10^{16}		3.18×10^{15}	5.65×10^{15}	1.79×10^{16}	
H_2O	2.00×10^{16}	2.83×10^{16}	4.49×10^{16}	5.04×10^{15}	7.11×10^{15}	1.27×10^{16}		1.42×10^{15}	2.25×10^{15}	4.00×10^{15}	
HCN	1.79×10^{16}	2.52×10^{16}	4.00×10^{16}	4.00×10^{15}	5.65×10^{15}	1.13×10^{16}		1.13×10^{15}	1.59×10^{15}	3.57×10^{15}	
NH_3	1.79×10^{16}	2.00×10^{16}	2.52×10^{16}	4.00×10^{15}	5.04×10^{15}	6.34×10^{15}		1.13×10^{15}	1.42×10^{15}	2.00×10^{15}	
H_2S	1.42×10^{16}	1.79×10^{16}	2.25×10^{16}	3.18×10^{15}	4.00×10^{15}	5.04×10^{15}		7.98×10^{14}	1.01×10^{15}	1.42×10^{15}	
SiO	2.25×10^{16}	3.56×10^{16}	5.65×10^{16}	5.04×10^{15}	1.01×10^{16}	1.79×10^{16}		1.59×10^{15}	3.18×10^{15}	5.65×10^{15}	
SiS	2.25×10^{16}	2.83×10^{16}	4.49×10^{16}	7.11×10^{15}	1.13×10^{16}	2.25×10^{16}		2.00×10^{15}	3.57×10^{15}	8.96×10^{15}	
CS	7.98×10^{15}	1.27×10^{16}	1.27×10^{17}	1.42×10^{15}	2.52×10^{15}	4.49×10^{16}		3.57×10^{14}	6.34×10^{14}	6.34×10^{15}	
HCl	1.79×10^{16}	2.25×10^{16}	4.00×10^{16}	4.00×10^{15}	5.65×10^{15}	1.13×10^{16}		1.01×10^{15}	1.59×10^{15}	3.57×10^{15}	
HF	3.18×10^{16}	4.49×10^{16}	5.65×10^{16}	1.01×10^{16}	1.27×10^{16}	2.00×10^{16}		5.04×10^{15}	7.11×10^{15}	8.96×10^{15}	
CO_2	2.25×10^{16}	3.18×10^{16}	6.34×10^{16}	5.04×10^{15}	7.98×10^{15}	1.79×10^{16}		1.59×10^{15}	3.18×10^{15}	7.11×10^{15}	
SO	1.59×10^{16}	2.83×10^{16}	4.00×10^{16}	3.57×10^{15}	7.11×10^{15}	1.13×10^{16}		1.01×10^{15}	2.25×10^{15}	4.00×10^{15}	
SO_2	1.59×10^{16}	2.25×10^{16}	3.56×10^{16}	3.57×10^{15}	5.65×10^{15}	1.01×10^{16}		8.96×10^{14}	1.59×10^{15}	3.18×10^{15}	
PO	2.52×10^{16}	4.00×10^{16}	6.34×10^{16}	7.11×10^{15}	1.27×10^{16}	2.25×10^{16}		2.25×10^{15}	4.00×10^{15}	7.98×10^{15}	
PN	2.00×10^{17}	5.04×10^{17}	1.01×10^{18}	8.96×10^{16}	2.52×10^{17}	1.01×10^{18}		4.00×10^{16}	1.13×10^{17}	5.65×10^{17}	

abundant daughters for all mass-loss rates and for C-rich and O-rich outflows. These are shown in Figs 7, D1, D2, D3, and D4.

A moderate negative correlation exists between peak fractional abundance and column density and their errors for all daughter species in both O-rich and C-rich outflows (RCCs between -0.39 and -0.53). The correlation is weak for the abundant C-rich daughters (RCC between -0.29 and -0.39). For the abundant O-rich daughters, the correlation is statistically non-significant, which could be due to the smaller number of abundant daughters (~ 25). We find a strong positive correlation between the dispersion of the peak fractional abundance and the dispersion of the column density (RCC ≥ 0.60), except for all C-rich daughters, which has a moderate correlation (RCC ~ 0.44). For each type of chemistry, the correlation is stronger for the abundant daughters than for all daughters.

APPENDIX E: CO RADIATIVE TRANSFER MODELS

The Mamon et al. (1988) prescription parametrises the CO abundance profile using

$$x(r) = x_0 \exp\left(-\ln 2 \left(\frac{r}{r_{1/2}}\right)^{\alpha}\right),\tag{E1}$$

with x the CO fractional abundance, x_0 its initial abundance, $r_{1/2}$ the radius in cm where its abundance is half its initial value, and α a measure of the profile's steepness. The values of $r_{1/2}$ and α used in the radiative transfer modelling, for the mass-loss rates and expansion velocities given in Table 1 and initial abundances given in Table 2, were retrieved using the equations described in Schöier & Olofsson (2001) and are listed in Table E1.

Radiative transfer models were calculated using the smallest and largest predicted CO envelope sizes (Table C1) along with the standard Mamon et al. (1988) sizes. This is illustrated in Fig. E1, which shows the CO abundance profiles and calculated lines for the O-rich outflow with $\dot{M} = 10^{-7} \text{ M}_{\odot} \text{ yr}^{-1}$. Table E2 lists the CO $J = 1 \rightarrow 0$ and $J = 2 \rightarrow 1$ integrated intensities and the mass-loss rates pre-

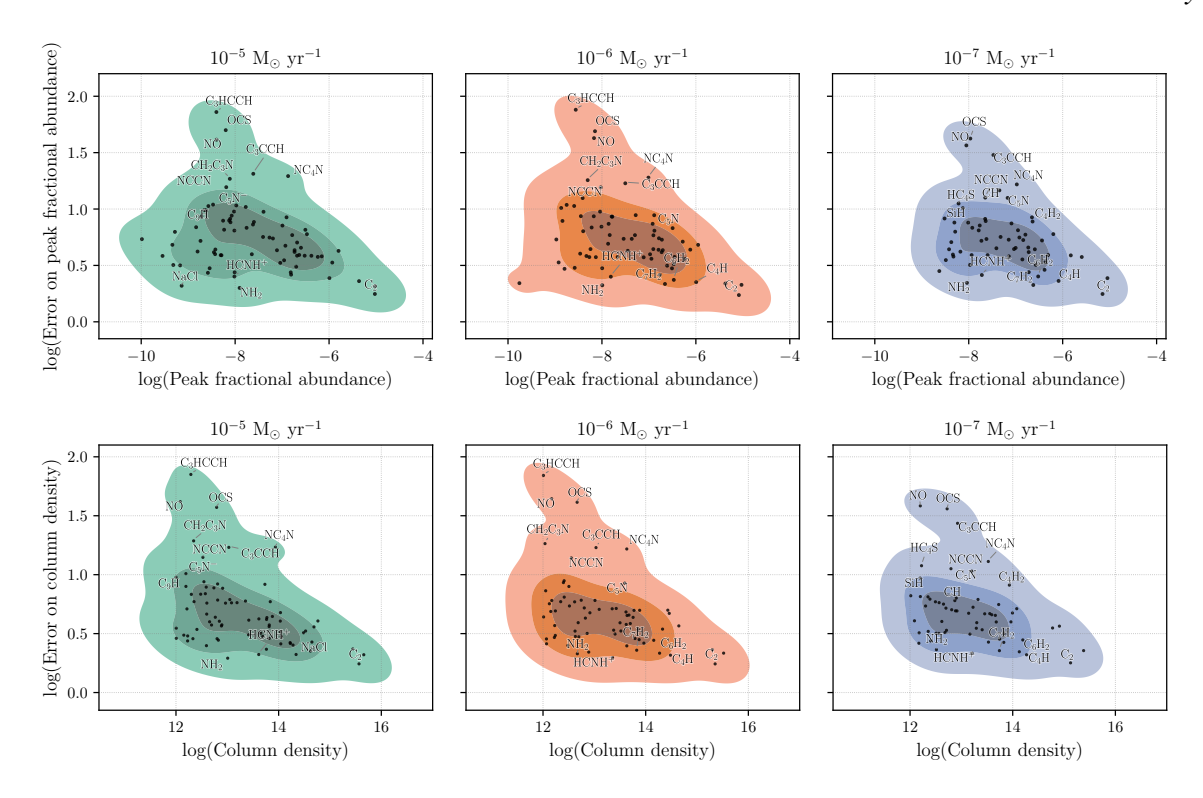


Figure D1. Scatter plots for all abundant species in C-rich outflows across all mass-loss rates. *Top:* mean peak fractional abundance versus the error on the peak abundance. *Middle:* mean column density versus its error. *Bottom:* dispersion of the column density versus the dispersion of the peak fractional abundance. Shaded contours show the kernel density estimation of the point distribution, with three intensity levels indicating regions of increasing point concentration. Least and most precise daughters(dispersion of both peak abundance and column density larger/smaller than their mean plus standard deviation) are labeled.

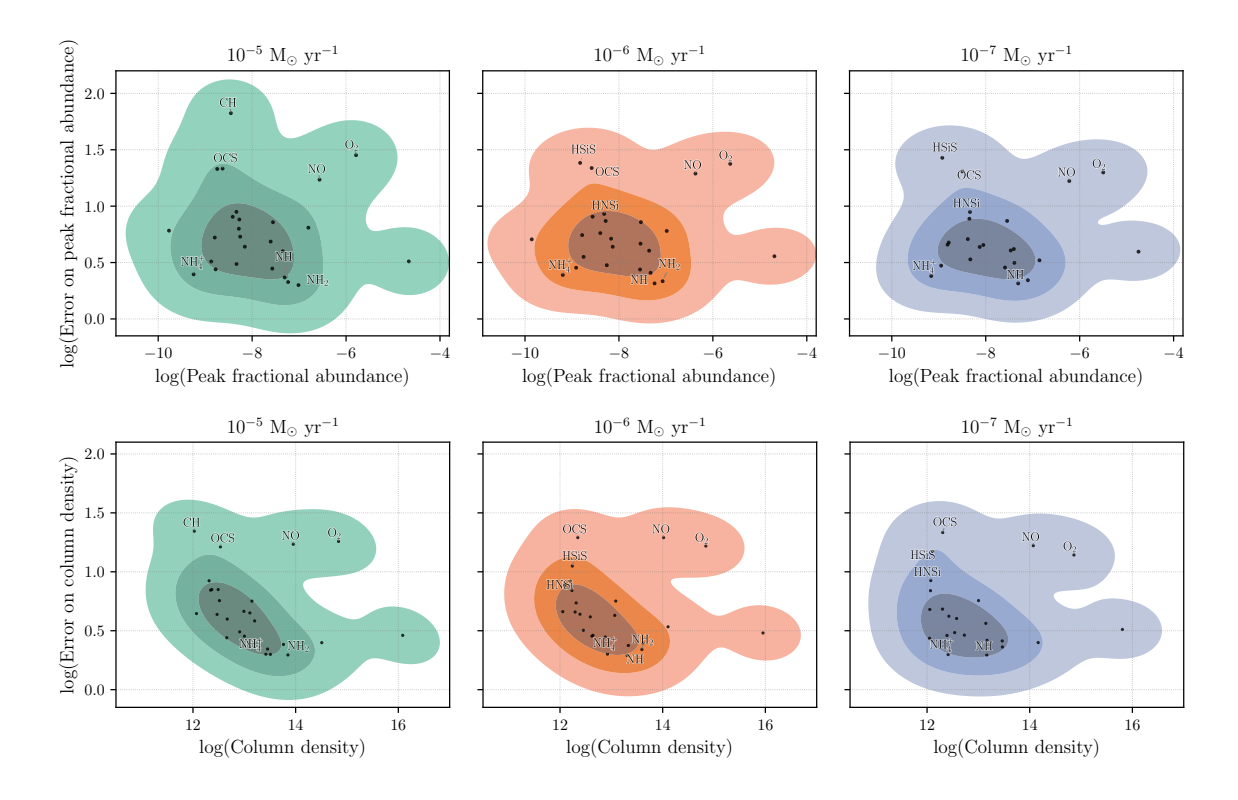


Figure D2. Same as Fig. D1, but for O-rich outflows across all mass-loss rates.

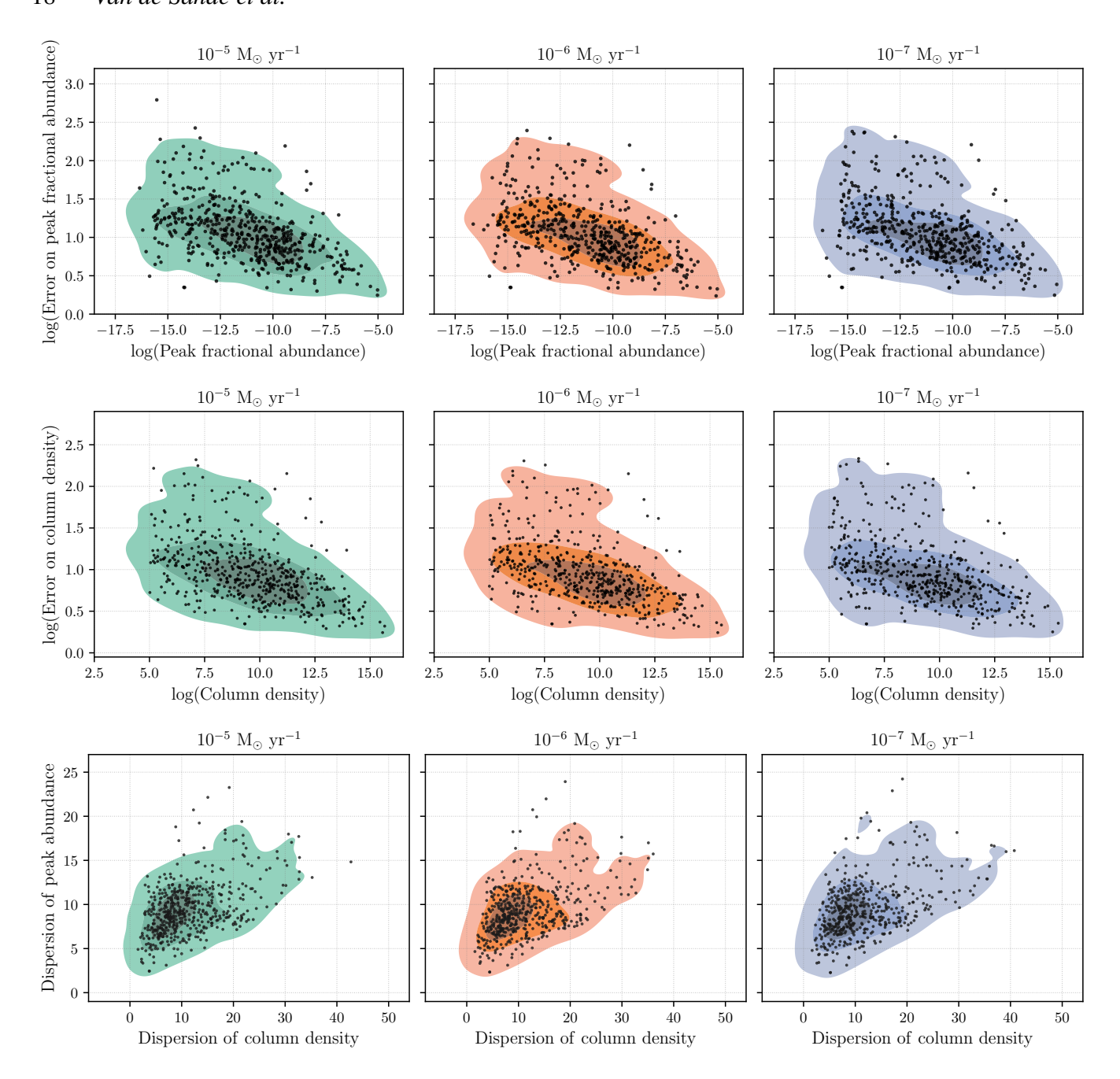


Figure D3. Scatter plots for all daughter species in a C-rich outflow across all mass-loss rates. *Top:* mean peak fractional abundance versus the error on the peak abundance. *Middle:* mean column density versus its error. *Bottom:* dispersion of the column density versus the dispersion of the peak fractional abundance. The daughter species have a column density $\geq 10^5$ cm⁻².

dicted from these values, along with the percentage difference of these values, determined as (predicted value from maximum extent - predicted value from minimum extent)/predicted value from Mamon et al. (1988).

This paper has been typeset from a TEX/IATEX file prepared by the author.

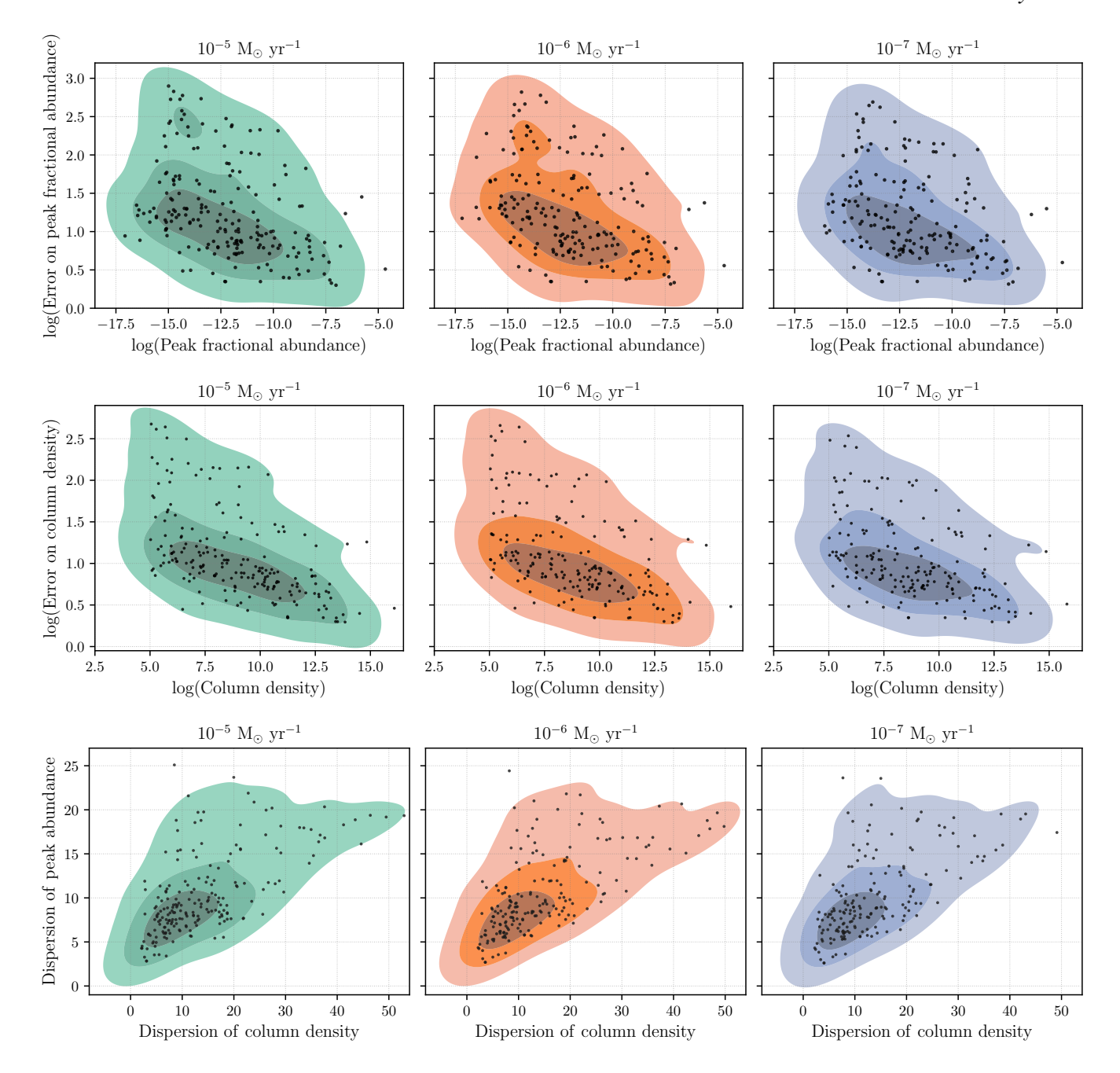


Figure D4. Scatter plots for all daughter species in a O-rich outflow across all mass-loss rates. *Top:* mean peak fractional abundance versus the error on the peak abundance. *Middle:* mean column density versus its error. *Bottom:* dispersion of the column density versus the dispersion of the peak fractional abundance. The daughter species have a column density $\geq 10^5$ cm⁻².

20 Van de Sande et al.

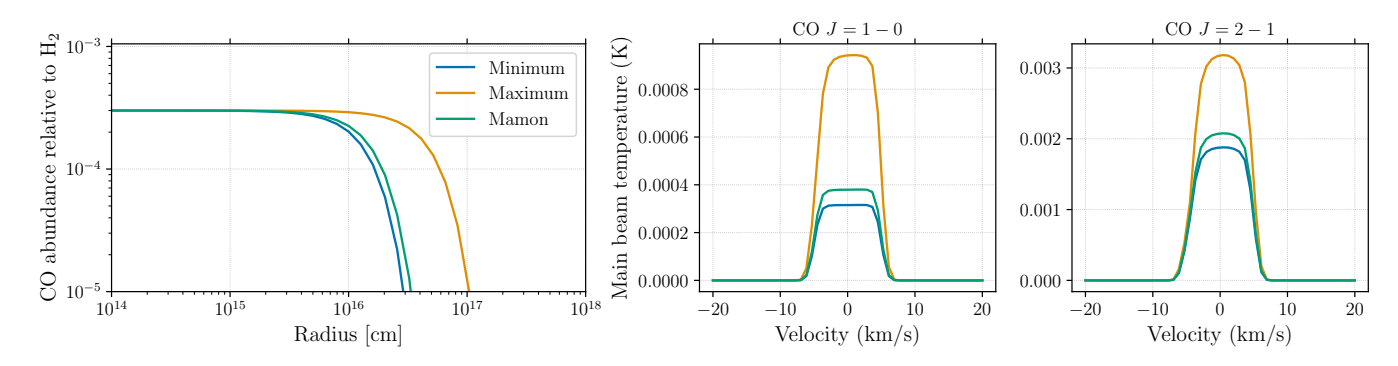


Figure E1. Left: CO abundance profiles used in the radiative transfer modelling of the O-rich outflow with $\dot{M}=10^{-7}~\rm M_{\odot}~\rm yr^{-1}$; the minimum and maximum predicted CO envelope sizes (Table C1) and the standard Mamon et al. (1988) size. Right panels: corresponding CO $J=1\to 0$ and J=2-1 line profiles calculated by the radiative transfer routine.

Table D1. Spearman rank correlation coefficients (RCCs) between the mean peak fractional abundance and its error (*top*), the mean column density and its error (*middle*), and the dispersion of the column density and the dispersion of the peak fractional abundance (*bottom*) for all daughters and abundants daughters for all mass-loss rates and for C-rich and O-rich outflows. p-values larger than 0.05 are boldfaced.

Mean peak fractional abundance - error peak fractional abundance								
M	RCC	p-value	RCC	p-value				
		Carb	on-rich					
		All	F	Relevant				
$10^{-5}~M_{\odot}~yr^{-1}$	-0.53	1.56×10^{-39}	-0.29	1.09×10^{-2}				
$10^{-6}~{\rm M}_{\odot}~{\rm yr}^{-1}$	-0.53	3.56×10^{-38}	-0.39	8.37×10^{-4}				
$10^{-7} \ {\rm M}_{\odot} \ {\rm yr}^{-1}$	-0.51	1.54×10^{-34}	-0.32	1.17×10^{-2}				
		Oxyg	gen-rich					
		All	F	Relevant				
$10^{-5}~{\rm M}_{\odot}~{\rm yr}^{-1}$	-0.46	1.02×10^{-11}	-0.08	6.82×10^{-1}				
$10^{-6}~{\rm M}_{\odot}~{\rm yr}^{-1}$	-0.44	1.56×10^{-10}	-0.07	7.45×10^{-1}				
$10^{-7}~M_{\odot}~yr^{-1}$	-0.39	5.26×10^{-08}	-0.17	4.46×10^{-1}				
M	ean colum	ın density - error d	column densit	у				
M	RCC	p-value	RCC	p-value				
		Carb	on-rich					
		All	F	Relevant				
$10^{-5}~{\rm M}_{\odot}~{\rm yr}^{-1}$	-0.54	2.48×10^{-41}	-0.47	1.72×10^{-5}				
$10^{-6}~{\rm M}_{\odot}~{\rm yr}^{-1}$	-0.55	2.46×10^{-42}	-0.43	1.81×10^{-4}				
$10^{-7}~M_{\odot}~yr^{-1}$	-0.53 2.22×10^{-38}		-0.37	2.27×10^{-3}				
		Oxyg	gen-rich					
		All	F	Relevant				
$10^{-5}~M_{\odot}~yr^{-1}$	-0.63	3.49×10^{-23}	-0.47	1.52×10^{-2}				
$10^{-6}~{ m M}_{\odot}~{ m yr}^{-1}$	-0.58	5.17×10^{-19}	-0.40	4.76×10^{-2}				
$10^{-7} \ M_{\odot} \ yr^{-1}$	-0.53	2.53×10^{-14}	-0.27	2.01×10^{-1}				
Dispersion of co	olumn den	sity - dispersion o	of peak fraction	nal abundance				
\dot{M}	RCC	p-value	RCC	p-value				
		Carb	on-rich					
		All	F	Relevant				
$10^{-5}~M_{\odot}~yr^{-1}$	0.44	4.60×10^{-27}	0.70	1.37×10^{-12}				
$10^{-6}~{ m M}_{\odot}~{ m yr}^{-1}$	0.44	1.07×10^{-25}	0.83	1.84×10^{-19}				
$10^{-7} \ M_{\odot} \ yr^{-1}$	0.44	6.96×10^{-26}	0.83	4.55×10^{-17}				
		Oxyg	gen-rich					
	·	All	F	Relevant				
$10^{-5}~M_{\odot}~yr^{-1}$	0.63	3.34×10^{-23}	0.79	1.58×10^{-6}				
$10^{-6}~{\rm M}_{\odot}~{\rm yr}^{-1}$	0.67	6.67×10^{-27}	0.80	1.47×10^{-6}				
$10^{-7}~{\rm M}_{\odot}~{\rm yr}^{-1}$	0.64	2.11×10^{-22}	0.81	2.78×10^{-6}				

Table E1. Values of $r_{1/2}$ [cm] and α of the Mamon et al. (1988) CO envelope size (Eq. E1) used in the radiative transfer modelling.

\dot{M}	$r_{1/2}$	α
Ca	rbon-rich	
$10^{-5} \ {\rm M}_{\odot} \ {\rm yr}^{-1}$	2.80×10^{17}	2.79
$10^{-6}~{ m M}_{\odot}~{ m yr}^{-1}$	8.13×10^{16}	2.35
$10^{-7} \ {\rm M_{\odot} \ yr^{-1}}$	2.46×10^{16}	2.04
Ox	ygen-rich	
$10^{-5}~{\rm M}_{\odot}~{\rm yr}^{-1}$	1.48×10^{17}	2.79
$10^{-6}~{ m M}_{\odot}~{ m yr}^{-1}$	4.44×10^{16}	2.35
$10^{-7} \text{ M}_{\odot} \text{ yr}^{-1}$	$t1.54 \times 10^{16}$	2.03

22 Van de Sande et al.

Table E2. Radiative transfer results for the C-rich outflows (top) and O-rich outflows(bottom), for all mass-loss rates (1st column) using the minimum and maximum extent (Table C1) and the Mamon et al. (1988) envelope size (Table E1, 2nd column). 3rd & 6th columns: integrated intensity of the CO $J = 2 \rightarrow 1$ and $J = 3 \rightarrow 2$ lines, respectively. 4th & 7th columns: percentage difference of the integrated intensities. 5th & 8th columns: predicted mass-loss rates based on these intensities, following Ramstedt et al. (2008). 6th & 10th columns: percentage difference of the predicted mass-loss rates. Percentage differences are calculated as (predicted value from maximum extent - predicted value from minimum extent)/predicted value from Mamon et al. (1988).

Mass – loss rate	Envelope size	$CO J = 1 \rightarrow 0$ [K km/s]	Ratio intensities	Predicted \dot{M}	Ratio \dot{M}	$CO J = 2 \rightarrow 1$ [K km/s]	Ratio intensities	Predicted \dot{M}	Ratio M
				Carbon-rich					
$10^{-5}~{\rm M}_{\odot}~{\rm yr}^{-1}$	Minimum Maximum Mamon	6.69×10^{-1} 6.69×10^{-1} 7.06×10^{-1}	0.00%	4.38×10^{-6} 4.38×10^{-6} 4.54×10^{-6}	-0.03%	1.57 1.57 1.57	0.00%	4.40×10^{-6} 4.40×10^{-6} 4.41×10^{-6}	0.00%
$10^{-6}~{\rm M}_{\odot}~{\rm yr}^{-1}$	Minimum Maximum Mamon	9.26×10^{-2} 1.38×10^{-1} 1.20×10^{-1}	37.50%	8.99×10^{-7} 1.18×10^{-6} 1.07×10^{-6}	25.92%	3.01×10^{-1} 3.53×10^{-1} 3.37×10^{-1}	15.60%	9.44×10^{-7} 1.08×10^{-6} 1.04×10^{-6}	12.87%
$10^{-7}~{\rm M}_{\odot}~{ m yr}^{-1}$	Minimum Maximum Mamon	1.10×10^{-2} 2.02×10^{-2} 1.34×10^{-2}	68.80%	1.40×10^{-7} 2.12×10^{-7} 1.60×10^{-7}	44.85%	4.33×10^{-2} 5.66×10^{-2} 4.75×10^{-2}	28.10%	1.40×10^{-7} 1.75×10^{-7} 1.51×10^{-7}	22.86%
				Oxygen-rich	l				
$10^{-5}~{\rm M}_{\odot}~{\rm yr}^{-1}$	Mininum Maximum Mamon	3.91×10^{-1} 4.65×10^{-1} 4.43×10^{-1}	16.70%	6.67×10^{-6} 7.50×10^{-6} 7.25×10^{-6}	11.50%	1.08 1.17 1.14	7.60%	5.79×10^{-6} 6.17×10^{-6} 6.07×10^{-6}	6.30%
$10^{-6}~{\rm M}_{\odot}~{\rm yr}^{-1}$	Mininum Maximum Mamon	1.08×10^{-1} 1.59×10^{-1} 4.23×10^{-2}	122.00%	2.18×10^{-6} 2.85×10^{-6} 1.16×10^{-6}	57.62%	3.38×10^{-1} 3.98×10^{-1} 1.58×10^{-1}	38.00%	1.85×10^{-6} 2.12×10^{-6} 9.93×10^{-7}	26.75%
$10^{-7}~{\rm M}_{\odot}~{\rm yr}^{-1}$	Mininum Maximum Mamon	3.14×10^{-3} 8.97×10^{-3} 3.77×10^{-3}	154.60%	1.31×10^{-7} 2.68×10^{-7} 1.48×10^{-7}	91.96%	1.73×10^{-2} 2.82×10^{-2} 1.90×10^{-2}	57.50%	1.18×10^{-7} 1.76×10^{-7} 1.27×10^{-7}	45.71%